University of Zurich[UZH]

Uncertainty Analysis for Input Parameters of the Atmospheric Compensation Process in Airborne Imaging Spectroscopy.

GEO 511 Master's Thesis

Author
Tina Gut
14-721-328

Supervised by
Dr. Andreas Hüni

Faculty representative
Prof. Dr. Michael Schaepman

30.09.2019
Department of Geography, University of Zurich

University of Zurich[UZH]

Department of Geography

Uncertainty Analysis for Input Parameters of the Atmospheric Compensation Process in Airborne Imaging Spectroscopy.

GEO 511 Master Thesis

Tina Gut
14 721 328

Supervisor: Dr. Andreas Hüni

Faculty Member: Prof. Dr. Michael Schaepman

Acknowledgements

Sincere thanks to Dr. Andreas Hüni who supervised and coached this thesis. Thank you for the many inputs, assistance and patience. Likewise, many thanks to Dr. Daniel Schläpfer who offered great support to me concerning all kinds of technical questions about the ATCOR and MODO software as well as advice with regards to contents. Additionally, I would like to thank Dr. David R. Thompson who offered his support for my originally intended thesis on parts of his current work.

Abstract

In airborne imaging spectroscopy for the Visible Shortwave Infrared (VSWIR) wavelength range the state of the atmosphere can have a large influence on the values detected by optical sensors like APEX or AVIRIS NG. Since the value of interest is the reflectance property of the surface, atmospheric effects need to be compensated for. Atmospheric compensation algorithms like ATCOR-4 use radiance images as input data. In theory, the algorithm would then estimates the hemispherical-directional reflectance factor as a function of radiance intensity minus the influence of atmospheric particles and processes. Assuming the atmospheric parameters to be independent of the radiance intensity, a higher obtained radiance would necessarily lead to a higher estimated reflectance factor. The atmospheric compensation, however, is not a linear function and therefore the resulting images might show errors. This thesis presents an uncertainty analysis for the radiance intensity as one of several independent and non-independent input parameters and variables of ATCOR-4. The analysis is done by modelling the radiance images with factors drawn from a normal probability distribution and simulating the corresponding reflectance factor images with consideration of various other parameters and variables. Generally, the resulting HDRF can be found to have a wavelength dependent standard uncertainty of 0 to 0.15% associated with the radiance intensity. The uncertainty values are put into perspective by showing how other factors like a) the solar reference spectrum, b) the solar azimuth and zenith angle, c) the sensor uncertainty, d) different steps within the atmospheric compensation process, e) the choice of terrain mode in ATCOR-4 and f) the adjacency effect do all have an influence on the HDRF as well.

List of Figures

List of Equations

Contents

1 Introduction

Before an image of reflectance factors can be used in order to explore the earth's surface it takes a series of steps to produce this product. At the beginning there stands a measurement process with a resulting measured value. These values are digital numbers about how many photons were sensed by the sensor for a certain time and area (pixel). The digital numbers then are calibrated with sensor specific calibration coefficients in order to convert them into radiances L with unit $[Wm^{-2}sr^{-1}]$ (Schaepman-Strub et al., 2006). The radiance values obtained at sensor level are then converted into reflectance factors by a radiative transfer code trough compensating for atmospheric effects in the signal (Richter & Schläpfer, 2016).

During the process of acquiring, processing and analysing spectroscopic data various sources of uncertainty can be identified. During the measurement process the instrument has to be calibrated according to instrument characteristics and methodology of measurement. Specifically, the resolution of the sensor and the spatial diversity of target properties can be a source of measurement variability (Hueni et al, 2016). Then, the raw data is converted from digital numbers to radiance values. For this conversion sensor and scene specific calibration coefficients are applied. Later on, the radiances are transformed into reflectances by an atmospheric compensation (Richter & Schläpfer, 2016). Hereby, assumptions about the state of the atmosphere are made and parameters are estimated in order to remove the part of the signal that is caused by the interaction of sunlight with the atmosphere. This radiometric correction as well as the spectral, geometric and instrument calibration are typical sources of uncertainty.

In order to analyse these uncertainties it is a key concept in Earth Observation Science to follow the guidelines of the QA4EO - Quality Assurance Framework for Earth Observation. Six of the seven guidelines attempt to explain the Guide to the expression of uncertainty in measurement (GUM). This guide was established by a group of meteorologists and the Bureau International des Poids et Mesures (BIPM). Those guides and guidelines are aiming for Earth Observation data and products to have a fully traceable indicator of their quality with them. The quality indicator is called QI and provides information for all users to allow them to evaluate the fitness and purpose of the data or product. Next to a QI, traceability is another key concept to assure and uniform proper data quality assignment. A traceability is supposed to be an unbroken chain of documented and quantifiable assessments of evidence for each step that was done with the data. The traceability chain should be expressed according to internationally agreed standards in an audited and peer reviewed way. Favourably, measurements should be done in SI (standard units).

For certain steps in the data processing chain it is relatively simple for a user to find the associated uncertainty. For example the instrument should actually be provided with a QI by the manufacturing company. Other steps are based on assumptions and estimations and are therefore not always unambiguously traceable. One example for a process who's uncertainty isn't fully understood yet is the atmospheric compensation. A standard atmospheric correction tool is ATCOR (Richter, 1998) which is based on the radiative transfer code of MODTRAN (MODTRAN-6 code (Berk et al. 2014)). ATCOR-4 estimates the irradiance on the ground from the radiances measured at the sensor and the database of MODTRAN. The software offers additional validation tools (Richter & Schläpfer, 2002). An other example for a more recently developed atmospheric compensation algorithm is "isofit" from Thompson et al. (2018). This is a procedure of compensating the atmosphere through a joint probabilistic formulation with a method called optimal estimation based on Rodgers et al. (2000). Hereby, the reference spectra as well as the usual atmospherical parameters can be included in the estimation of the hemispherical-directional reflectance factor of the surface. The uncertainty associated with the result of the compensation can be provided along with the estimators.

Accurate atmospheric compensation for as many surface types as possible is an important goal for today's imaging spectroscopy (Gao et al., 2009). Especially for airborne campaigns reliant uncertainty values are crucial in order to make different studies comparable. Not only is it necessary to get area-wide coherent results but also should it be possible to estimate quantities for different regions of the earth's surface with the same uncertainty and quality standards. In this thesis the focus lays on airborne optical image data and the uncertainty associated with the radiance intensity that serves as input to ATCOR-4. The study site is the town Wettingen in Switzerland for which an extensive campaign has been run in July 2018 by overflying the area with two different sensors (APEX and AVIRIS NG) and simultaneously measuring the reflectance factors on the ground with an ASD field spectrometer. The goal of atmospheric compensation however should be to extend studies like this for many other (until now underrepresented) study sites in other regions like for example tropical forests or coastal regions (Thompson et al., 2019).

In order to get there, a constant convergence of atmospherically compensated reflectance factors to in situ measurements is the step by step cycle of reducing the uncertainty associated with atmospheric compensation algorithms. It is therefore obvious to wonder about how this uncertainty associated with the result of for example ATCOR-4 is composed and which parameters are crucial for the improvements. So, in the following thesis I will present the basics of airborne remote sensing radiative transfer as well as the basics of uncertainty analysis. This theory section is terminated by a literature review on uncertainties in atmospheric compensation and followed by the above mentioned uncertainty analysis for the test images of Wettingen from APEX and AVIRIS NG processed by ATCOR-4. In addition to the question of how the intensity of the radiance values affects the estimated hemispherical-directional reflectance factor other input variables of ATCOR-4 are simulated and analysed on their associated uncertainty. This will complete the uncertainty analysis by including systematic errors as well as correlations between the radiance intensity and other factors.

2 Theoretical foundations

2.1 The principles of atmospheric compensation

Remote Sensing in the visible (VIS) to shortwave infrared (SWIR) wavelength range is the science of radiometric analysis of the surface's reflected radiance between 0.4 to 2.5 um. The quantity reflectance however is not per se measurable. It can only be approximated from radiance measurements. The measured radiometric quantity obtained by imaging spectrometers is radiance reflected by the surface. In order to obtain the amount of radiance a sensor has to count photons (energy). A radiometric measurement device records photons per time interval. Spectroradiometry therefore is the measurement of energy per time per wavelength. The total energy transfer by radiance then is calculated as the number of photons times the photon's energy and is called radiant flux (unit $[W = J/s]$). When observing the reflectance properties of a surface the 'reflectance' is defined as in equation 1. According to this definition, the 'reflectance' of a surface is a characteristical ratio and hence independent of illumination intensity, time and place. It is however a function of wavelength and a function of view angle.

$$\rho = \frac{\text{outgoing (}\textit{reflected}\text{) radiant flux [W]}}{\text{incoming (}\textit{incident}\text{) radiant flux [W]}} \tag{1}$$

The path of the photons from the Sun towards the earth, through the planet's atmosphere, over the surface, again through the atmosphere and eventually into the sensor is long and complex. A variety of models try to illustrate different parts of this path. The focus of this thesis lies on the atmospheric compensation, which is the part of inverting the atmospheric influence of the spectral radiance obtained at the sensor in order to estimate surface properties. In the following section the most (for atmospheric compensation) relevant concepts and models of imaging and field spectroscopy will be presented. The uncertainties associated will be mentioned along with the principles of each presented physical quantity and step in the process of radiometric analysis. This should be an introduction and orientation for the subsequent chapter on the principles of uncertainty analysis.

2.1.1 Solar irradiance reference spectrum

The first model in a long line of models is about the sun as a source of energy. The sun's power radiated per area is calculated as $62.84 W/m^2$ while the sun is assumed to be a black body. With a model of the sun's exitance it's possible to estimate the radiance distribution and luminance arriving at the top of the earth's atmosphere. This is done by finding a solar irradiance reference spectrum. A solar spectrum describes the sun's radiant flux dependent on wavelength. Typically, the exoatmospheric solar irradiance is defined as E_0. As described in equation number 2 the extraterrestrial irradiance is given as the radiant flux (total energy transfer through radiation) of the sun per surface area. In expression 2 $d\Phi_0$ is the incident solar radiant flux on top of the atmosphere and $dA_\perp$ stands for the incident unit area with an irradiance angle perpendicular to the surface area. The incidence angle φ of the sun rays can be assumed to be parallel within a deviation of 0.5 degrees of the sun's disk size. The size of the unit area varies within one year within 6% m^2. As defined in equation 3, area $dA_\perp$ (and so does E_0 accordingly) depends the sun-earth distance D which varies between 1.47110^{11}m at aphelion and $1.52110^{11} m$ at perihelion and is averaged as one astronomical unit AU.

$$E_0 = \frac{d\Phi_0}{dA_\perp} \; [W/m^2] \tag{2}$$

The solar irradiance is the value for how much watt per square meter arrive at the top of the earth's atmosphere. In standard literature the unit area $dA_\perp$ is not differentiated for the two situations of bottom and top of atmosphere. Taking the radius of the earth as $r_{earth} = 6.371\ 10^6\ m$ and the radius of the earth plus its atmosphere as approximately $r_{earth+atm} = 6.371\ 10^6\ m + 100\ km = 6.471\ 10^6 m$ makes a difference in the resulting value of the unit area. For the standard unit area which isn't including the atmosphere the result is $dA_\perp = 8.837045\ 10^{23} m^2$. For a version with consideration of the atmosphere as in equation 3b the resulting area is $dA_{\perp,atm} = 8.837035\ 10^{23} m^2$. This is an absolute difference of $10^{18} m^2$ or 0.0003 % relative difference and a first example, of how uncertainty can be caused by unclear definitions (for calculations steps see Appendix).

$$dA_\perp = \frac{4\pi\ \left((D_{aph} - r_{earth})^2 + (D_{per} - r_{earth})^2\right)}{2}\ [m^2] \tag{3a}$$

$$dA_{\perp,atm} = \frac{4\pi\ \left((D_{aph} - r_{earth+atm})^2 + (D_{per} - r_{earth+atm})^2\right)}{2}\ [m^2] \tag{3b}$$

The spectral variability of the sun's irradiance is a function of wavelength with generally higher values toward shorter wavelengths. For the analysis of how the solar irradiance interact with the earth's atmosphere it is necessary to have a solar irradiance spectrum from XUV to infrared. Since no sensor is able to measure the entire spectrum, a composite of several sensors is required. The choice and composition of the different sensors is one of the reasons why different models of the sun can produce different reference spectra. The measurements take place on top or outside of the atmosphere to avoid including scattering and absorption processes of the earth's atmosphere. The main systematic errors of models of solar irradiance happen due to instrument calibration (Thuillier et al., 2004). The sensor calibration of a space-based measurement is especially challenging since some effects of the post-launch calibration rely on in-flight validation and on updates. To characterise changes during the flight, radiometric reference spectra can be provided on board by using calibrated lamps. Additionally, a diffuser can be placed in front of the sensor to see how the sensor was affected. A third option is to choose certain reference spectra in advance and compare the response of black bodies before the launch, after the launch and over time during the flight (online course uncertainty). An additional variability exists due to the solar cycle. In a period of 22 years the radiant intensity varies due to the amount of sun spots which are cooler than the rest of the sun's photosphere. This has a slight influence on the amount of energy that leaves the sun (Schühle et al., 2000). Typically used solar irradiance reference spectra are Thuiller (2004) and Fontenla (2011). The difference in radiance between those two solar spectra can be up to 5% (course Schläpfer, 2014).

2.1.2 Direct and indirect irradiance

The path of photons from the sun towards the surface of the earth and into the optical sensor crosses the earth's atmosphere twice; downward (suffix *down*) and upward (suffix *up*). Within the atmosphere some photons interact with particles like gases, aerosols and water. The irradiance that arrives at the surface after passing the atmosphere downward is defined as $E_g\ [W/m^2]$ and can be divided into a direct and a diffuse component. The component which is presented first is the direct, non-scattered flux through the atmosphere. The direct irradiance of a Lambertian and flat surface is defined as E_{dir} and described in the following equation 4a. A Lambertian surface is an ideal diffuse reflector. The reflectance factor for a Lambertian surface is a constant for all directions.

$$E_{dir} = \tau_{dir}\ E_0\ cos\theta_{il} \tag{4a}$$

$$E_{dif} = \left(\frac{\tau_{dif} + \tau_{dir}\ \overline{r_{DHR,adj}}\ \rho_{atm}}{1 - \overline{r_{BHR,adj}}\ \rho_{atm}} \right) E_0\ cos\theta_{il} \tag{4b}$$

$$E_g = E_0\ \tau_{down}\ cos(\varphi) + E_0\ \tau_{down,\ dif}\ V_{sky} + E_{ter} \tag{4c}$$

Expression number 4a shows E_{dir} as the fraction the extraterrestrial solar irradiance E_0 that arrives at the surface without scattering. This fraction depends on the direct transmittance of sunlight through the atmosphere τ_{dir} and the cosine of the solar illumination zenith angle $cos(\theta_{il})$. The top of atmosphere irradiance E_0 is derived from the earlier mentioned solar irradiance reference spectrum. The zenith angle of illumination $cos(\theta_{il})$ is defined through zenith and azimuth angle of the sun rays as well as zenith and azimuth angle of the surface normal vector (Hüni et al., 2016) as illustrated in figure 1. To calculate the solar zenith and azimuth angle the exact date and time is crucial. Whereas for the extraction of the surface normal vector a digital elevation model can be used.

The transmittance τ_{dir} in equation 4a is a function variable for the state of the atmosphere. In this case, the transmittance refers only to the direct flux. For a vertical path through the atmosphere the atmospheric transmittance is defined as $\tau_{dir} = e^{-\delta}$. In this definition δ represents the optical thickness and is calculated as the path length through the atmosphere multiplied by an extinction coefficient. Hereby, δ is the total optical thickness composed as $\delta_{\text{molecular scattering}} + \delta_{\text{aerosol}} + \delta_{\text{molecular absorption}}$. The optical thickness for molecules can be calculated as a function of pressure. The main part however are the aerosols. The Aerosol Optical Thickness AOT is taken at 550 nanometers $[nm]$ (ATCOR-4 manual).

The second component of the natural irradiance consists of the diffuse flux up- and downward the atmosphere. This diffuse flux is composed of scattering by the atmosphere and the adjoining area and objects of the observed surface. The diffuse irradiance component for a Lambertian and flat surface therefore depends on the state of the atmosphere and the topology. The entire amount of scattering in the atmosphere and at the adjacent areas is summed in E^{dif}.

Similar to the direct irradiance, the diffuse irradiance at sensor level is calculated by the extraterrestrial irradiance multiplied by the diffuse sunlight transmittance τ_{dif} and the cosine of the solar illumination zenith angle (equation 4a). The incoming diffuse irradiance depends as well on the fraction of radiance that has been reflected by the surrounding area and atmosphere and scattered towards the observed surface. The reflectance properties of the atmosphere is included by the spherical albedo ρ_{atm}. It is often referred to as the 'reflectance' of the atmosphere. The definition of reflectance as described in equation 1 is therefore applicable as well. The many different ways, a surface can scatter incoming radiance is characterised with the spatially homogenised spectral albedo $\overline{r_{BHR,adj}}$ and $\overline{r_{DHR,adj}}$ for the surrounding area. The spectral albedo ρ describes the reflectance properties of a surface when the incident radiation is monochromatic (as a function of wavelength λ) (Hueni et al., 2016). The spectral albedo is often referred to as bihemispherical reflectance (BHR) or directional-hemispherical reflectance (DHR) which will be further elaborated in section 2.1.3.

$$\rho = \frac{\Phi_r}{\Phi_i} = \frac{L_g \pi}{E_g} \tag{5}$$

As presented in equation 5 the spectral albedo of a Lambertian surface is defined as ratio between hemispherically reflected radiation on the ground and total radiance arriving on the ground. Often, the incident radiation is assumed to be isotropic (diffuse). In equation 5 $L_g = \Phi_r/\pi$ is the radiance reflected on the ground and $E_g = \Phi_{il}$ the total solar irradiance (diffuse and direct) arriving on the ground as described in equation 4c. Referring to equation number 4c τ_{down} is the total downward transmittance (direct and diffuse), $\tau_{down,\,dif}$ is the diffuse downward transmittance, φ stands for the incidence angle of solar flux and V_{sky} represents the skyview factor (the angle of effectively seen sky compared to a full hemisphere, defined as $\beta/2\pi$ (figure 1)). The radiance reflected by surrounding surface elements and onto the target surface is E_{ter} (Schläpfer, 2018, p.15).

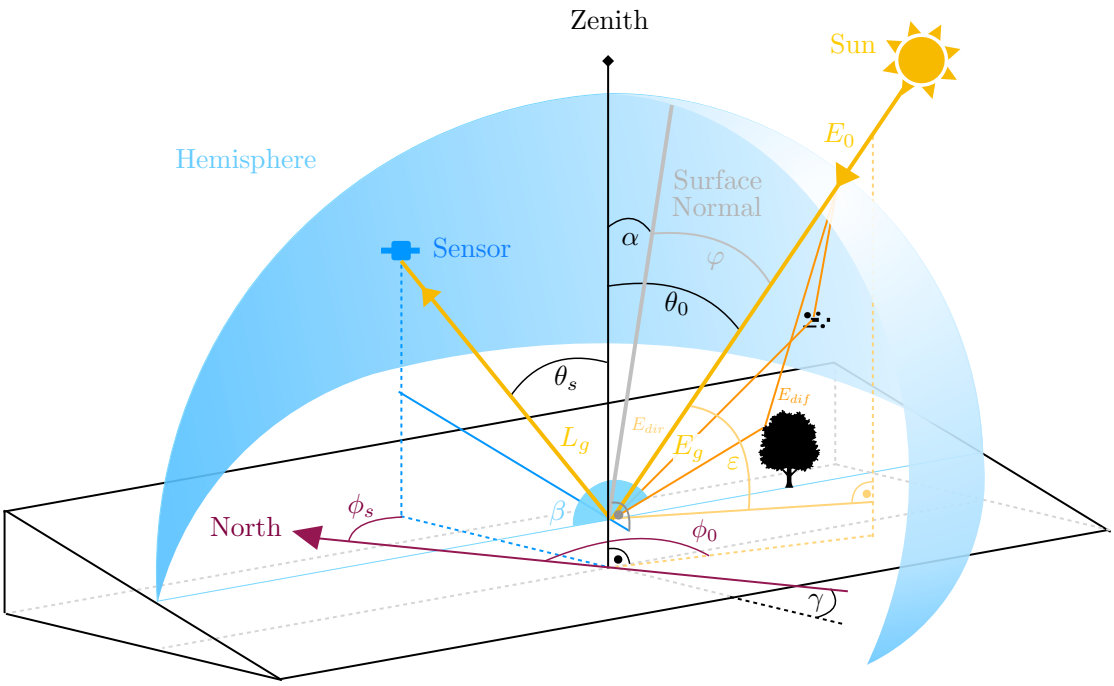

Figure 1: Standard angles in remote sensing data acquisition for a tilted surface with exemplary radiance and irradiances for that particular scene. The tree symbolises adjacent objects of the surrounding area and the points and lines in the air symbolise particles like aerosol or water vapour in the atmosphere. The sensor is an airborne pushbroom imaging spectrometer flying with the sky-blue line symbolising the along-track direction. The geographic direction North is marked with a dark-red line and arrow in order illustrate the azimuth angles. The Zenith is the normal vector of the horizontal plane for the surface. The surface normal vector is perpendicular to the tilted surface plane. The light-blue curves indicate a hemisphere above the surface which could in this case be seen as the atmosphere for the purpose of illustrating E_0. The scales however are not intended to be realistic.

2.1.3 Reflectance properties of the topology

In equation 5 the surface is assumed to be Lambertian (factor π). In reality, the surface is never an ideal diffuse backscatterer and the illumination is never perfectly directional or diffuse. The ratio of diffuse to direct irradiance is a function of wavelength with unit $[W\ m^{-2}\ nm^{-1}]$. Therefore, effects caused by different directional

Geometry		Radiation	
φ	incidence angle	E_0	extraterrestrial solar irradiance
ε	solar elevation angle	E_{dir}	direct radiant flux per m^2
θ_0	solar zenith angle	E_{dif}	diffuse radiant flux per m^2
ϕ_0	solar azimuth angle	E_g	total ground irradiance
θ_s	sensor zenith angle	L_g	ground reflected radiance
ϕ_s	sensor azimuth angle		(directed towards sensor)
α	terrain slope		
γ	terrain aspect (exposition)		
β	skyview angle		

properties of the surface show a high spectral dependence and need to be accounted for when determining the radiance of a scene (Schaepman-Strub et al., 2006). The assumption of the Lambertian surface is often kept in favour of faster calculation times. However, the surface reflectance needs to be described by the relation of reflected to incoming radiance for different illumination conditions. Therefore, other factors of the diffuse irradiance in equation **??** are the spatially homogenised directional-hemispherical reflectance $\overline{r_{DHR}}$ and the bihemispherical reflectance $\overline{r_{BHR}}$. Because of the atmospheric scattering these reflectance factors are required as well for the surrounding pixels.

The spectral albedo is of interest for imaging spectroscopy as it is independent of the sensor geometry. For blue-sky (ambient) illumination conditions the surface spectral albedo is influenced by the combination of diffuse and direct irradiance. In order to find a value for the spectral albedo, the reflectance properties of the surface can be approximated by combining different reflectance models. Typically, the bihemispherical reflectance (BHR) for diffuse illumination conditions (white-sky albedo) and the directional-hemispherical reflectance (DHR) for direct illumination (black-sky albedo) are linearly combined for this purpose. The BHR is defined as $BHR = \rho(2\pi, 2\pi)$ and describes the pure bihemispherical reflectance value for a perfectly diffuse irradiance. The BHR is a constant since it does neither depend on the solar geometry, nor the sensor geometry (Schläpfer, 2018). The directional-hemispherical reflectance DHR describes the reflectance for an almost perfectly directional illumination. Hereby, the angle of direct irradiance is again assumed as within a 0.5 degrees of the size of the solar disk. In mathematical terms $DHR = \rho(\theta_{il}, \phi_{il}, 2\pi)$ (Schläpfer, 2018). So, if the BHR for pure diffuse and the DHR for pure directional illumination are compared, the albedo includes the ratio of diffuse to direct illumination. This ratio is wavelength dependent because of the Mie and Rayleigh scattering mechanisms. So, the combination of BHR and DHR should be calculated for every band. Likewise, it is recommended to include the solar geometry when describing the spectral albedo because of the dependence on the illumination angle of the direct component (Schaepman-Strub et al., 2006).

To derive the spectral albedo from directional reflectance values is the task of the bidirectional reflectance distribution function (BRDF). The $BRDF(\theta_{il}, \phi_{il}; \theta_r, \phi_r; \lambda)$ describes how radiance from one direction in the hemisphere is scattered at the surface into another direction in the hemisphere. It is a function of incidence angle $cos(\varphi)$ and of the observation angle and is wavelength-dependent. The irradiance is assumed to be a parallel beam for this purpose (Schläpfer, 2018, p. 18). The illumination and reflectance angles are defined as θ_{il}, ϕ_{il} zenith & azimuth angle of incoming radiation and θ_r, ϕ_r zenith & azimuth angle of reflectance.

Of course, how much of the reflected radiation arrives at the sensor depends on where the instrument is and

in which direction the sensor faces (the sensors incident field of view iFOV). The view angle of an airborne sensor can have a large variety depending on the sensor's scan angle, the position of the target within the field of view, the topology and the altitude of flight. For rugged terrain like mountains the BRDF effect can be especially strong. Some slopes might be facing the sun and others might be facing away and lay in the shadow. The pixels of opposite view angle then show a significantly lower brightness for the same surface types compared to slopes facing the sun. In a simple approach, the BRDF compensation takes place as an across-track illumination correction. Each pixel across the beam gets its own correction factor according to the scan angle. For a more complex model the view angle is added to the model of the scan angle by considering the terrain. In an even more elaborated approach (this is the standard procedure in ATCOR-4) the surface type, the time of the year (geometry of solar illumination) and the spectral dependence get included as well. In this case the image gets corrected with an index for each pixel's theoretical anisotropy factor K as in equation number 6a (ATCOR-4 manual).

The BRDF compensation happens after the atmospheric compensation (sections 2.1.5-7). So, this is an anticipated section. The output of the atmospheric compensation is the in-field hemispherical-directional reflectance (HDR) of the surface, also known as bottom of atmosphere reflectance ρ_{boa}. This parameter describes the fraction of the hemispherical (diffuse) incident illumination reflected on the surface and directed towards the instrument. In order to receive the searched anisotropy factor per pixel the measured hemispherical-directional reflectance factor $HDRF_{measured}$ is set in relation to the spectral albedo BHR (equation 6a). The measured hemispherical-directional reflectance factor is dependent on wavelength. It includes the direct and diffuse irradiance from the whole hemisphere and therefore the state of the atmosphere and the surrounding terrain and is defined as $HDRF_{measured} = BRF\ d + HDRF\ (1-d)$. Hence, the measured HDRF can be divided into a directional (bidirectional reflectance factor (BRF)) and isotropic (HDRF) component. In other words, the received bottom of atmosphere reflectance factor is described for the situation of direct plus diffuse illumination. The BRF describes the ratio of the reflected radiant flux for an area to the reflected radiant flux of a Lambertian surface with the same area, illumination conditions and observation angle. For an ideal diffuse scatterer the BRDF is constant at $\frac{1}{\pi}$. The BRF of an ideal diffuse surface is $\frac{\pi}{\pi} = 1$. So the bihemispherical reflectance distribution function is related to the bihemispherical reflectance factor as $BRF[unitless] = \pi BRDF\ [sr^{-1}]$.

$$K = \frac{HDRF_{measured}}{BHR} = \frac{BRF(\theta_{il}, \phi_{il}; \theta_r, \phi_r)\ d + HDRF(\theta_r, \Delta\phi)\ (1-d)}{BHR} \tag{6a}$$

$$d = \frac{E_{dir}}{E_g} \tag{6b}$$

The parameter d represents the fraction of direct irradiance at surface level and is described in equation 6b as the fraction of direct irradiance per total irradiance arriving at the surface. Therefore, the fraction of diffuse irradiance at the surface is $(1-d)$ when the total ground irradiance is approximated as $E_g = E_{dir} + E_{dif}$. The factor d is applied to the BRF since it describes the directional part of the illumination and the factor $(1-d)$ corresponds to HDRF, the diffuse illumination fraction.

Summarised, especially the in-field hemispherical-directional reflectance of rugged terrain needs to be compensated for different view angles as well as diverse illumination conditions for different surface types. Assuming the surface to be a Lambertian backscatter is never true for a real scene. But this assumption can be used as an approximation in order to have shorter calculation times. In the case of a Lambertian surface the different kinds of reflectance like hemispherical-directional, directional-hemispherical, and hemispherical-

hemispherical reflectances are all equal to the surface reflectance ρ_s (surveys in geophysics). Also, the underlaying assumption of a pure directionally independent, diffuse illumination may not be accurate and might therefore cause significant uncertainties. The actual sky conditions might be a mixture of different kinds of illumination. So technically, the denominator in equation 6a should be the complete spectral albedo (including the DHR) and not only the BHR for diffuse illumination. But then the anisotropy factor would depend on the illumination angle which would cause the factor to be a function and the calculating time to be enlarged. However, in the BRDF correction the assumption often causes an over-correction for weakly illuminated areas with large view angles (ATCOR-4 manual).

2.1.4 Sensor-, Data- and Spectral Calibration

Radiometric Calibration of the sensor

The most important uncertainties in imaging spectroscopy are linked to the instrument and its application. Generally, the instrument records at a spectral range of 0.4 to 2.5 um. At the sensor, the directional radiance signal is recorded in digital numbers DN per band as a measure of how many photons arrive at the sensor for each wavelength. The recording takes place at detector level where electrons are being amplified and digitised. After the data is stored, data calibration as in equation nr. 7a is required to transform the measured number (DN) into a physical quantity. For an imaging or field spectrometer this physical quantity is the spectral radiance L with unit $[W\ m^{-2}\ sr^{-1}\ nm^{-1}]$ defined as power per area per angle per wavelength. This process is called Radiometric Calibration and has to be done for each band.

As presented in equation 7a the measured radiance of a scene L_{scene} is calculated by the obtained digital number for that scene and sensor $DN_{\text{sensor, scene}}$ multiplied by the gain of the instrument G_{sensor} and added to the origin radiance offset L_0. To obtain the gain of the sensor (equation 7b) the following calibration steps are required: The aim is to calibrate the instrument in a fully traceable way by having SI units wherever possible. At the end, the instrument should come with a calibration certificate including an uncertainty in %. At the beginning of the calibration chain stands a lamp and diffuser serving as reference radiance L_{source} (for APEX this comes from RASTA, the organisation that is responsible for the certificates). A reference spectrometer measures the radiance of the reference lamp by recording digital numbers for several bright and dark readings (for APEX this is a SVC transfer spectrometer). The average of several bright minus the average of several dark readings is summed in DN_{source}. The fraction of $\frac{L_{\text{source}}}{DN_{\text{source}}}$ is then the gain of the reference spectrometer G_{ref} for every wavelength and has the unit $\left[\frac{W}{m^2 * sr * nm * DN}\right]$.

$$L_{\text{scene}} = G_{\text{sensor}} * DN_{\text{sensor, scene}} + L_0 \tag{7a}$$

$$G_{\text{sensor}} = \frac{\left(DN_{\text{sphere}}\ \frac{L_{\text{source}}}{DN_{\text{source}}}\right)\tau_{\text{filter}}}{\left(DN_{\text{sensor, cal}}\right)} \tag{7b}$$

$$DN_{\text{sensor, scene}} = DN_{\text{sensor, scene, bright}} - DN_{\text{sensor, scene, dark}} \tag{7c}$$

As a next step the transfer (or reference) spectrometer takes several readings of DNs using an integrating sphere source. The radiance of the sphere is calibrated as $L_{\text{sphere}} = DN_{\text{sphere}} G_{\text{ref}}$. Again, the DNs are obtained as the average of bright minus average of dark readings. After being calibrated, it is possible to use the sphere

as reference for a variety of sphere-filter combinations measured by the original sensor (the one that gets used in the field). In order to get the sensor response for different signal levels, the digital numbers per wavelength are obtained through radiance measurements of different filters with repeated bright and dark readings each. As a result, $DN_{\text{sensor, cal}} = DN_{\text{sensor, cal, bright}} - DN_{\text{sensor, cal, dark}}$ is obtained for each wavelength and a variety of τ_{filter} signal levels. Now, it is possible to calculate the slope G_{sensor} and origin offset L_0 of the sensor with a straight line calibration. When finally reading a scene with the calibrated instrument, the digital numbers per band $DN_{\text{sensor, scene}}$ are again calculated as average of several bright minus average of several dark readings as written in equation 7c. After the instrument has measured a scene it is possible to adapt the calibration coefficients to a higher order if needed. The straight line calibration serves as a first guess and is usually sufficient (uncertainty textbook).

Spectral Convolution

In practice, one sensor-band doesn't measure at one single wavelength. The real measured value is an equation like the spectral convolution in expression number 8. A spectral convolution transforms the data calibrated DNs into a weighted integral of the scene radiance per wavelength. So, at the end a new DN is calculated as a spectrally re-sampled value of the scene radiance per wavelength. The new DN $DN_{\text{sensor, scene, new}}$ can be described as a function of a weighted average. The re-sampling -or weighting- is done by a spectral response function (SRF). A SRF describes the sensitivity of an instrument. The sensitivity is also called responsivity and shows how accurately the instrument measures per band. Often, the SRF is approximated by a normal distribution and characterised by the centre wavelength λ_0 as presented in figure 2. Other characteristics of a SRF are the Full Width at Half Maximum (FWHM) and the spectral sampling interval (SSI). The FWHM is called the spectral resolution since it describes the deviation of the Gaussian curve from the mean centre wavelength. The SSI is defined as the distance between two neighbouring centre wavelengths and can be seen as the 'real' spectral sampling interval of an instrument. In equation 8 $R_{\text{sensor,SRF}}(\lambda;\lambda_0)$ represents the SRF for a pixel centred on wavelength λ_0 for every sample wavelength λ.

$$DN_{\text{sensor, scene, new}} = \int R_{\text{sensor, SRF}}(\lambda;\lambda_0)\, L_{\text{scene}}(\lambda)\, d\lambda \tag{8}$$

In figure 2 all simulated SRFs show the same spectral resolution and their centre wavelengths correspond quite exactly to the average wavelength of the band. This is not necessarily the case across the whole spectrum. What one can't see in figure 2 is how along the spectrum the FWHM as well as the centre wavelength might increase non-linearly. The instrument might actually be a composite of different sensors. Or the spectral response function might as well not the same for every pixel across track. By plotting the central wavelength against the nadir wavelength for every across track position it is possible to see how the obtained radiance values can differ within the same band. The same object might be recorded with a significantly different radiance value depending on where across track it is located. This effect is called smile effect and might still not disappear after the convolution. It is best visible for absorption feature bands like the 760 nm oxygen a band. The fact that the sensor response isn't uniform across track is typical for pushbroom imaging spectrometers. The effect can be compensated for during the atmospheric compensation process.

The SRF is found by scanning a spectrally tuneable laser across a spectral response region of interest and a little beyond (a band and its contiguous wavelenghts). The response of the spectrometer at each wavelength of the laser measurement is either compared to a reference detector or obtained with a reference source of illumination. The reference detector has a known spectral response. The reference lamp emits monochromatic

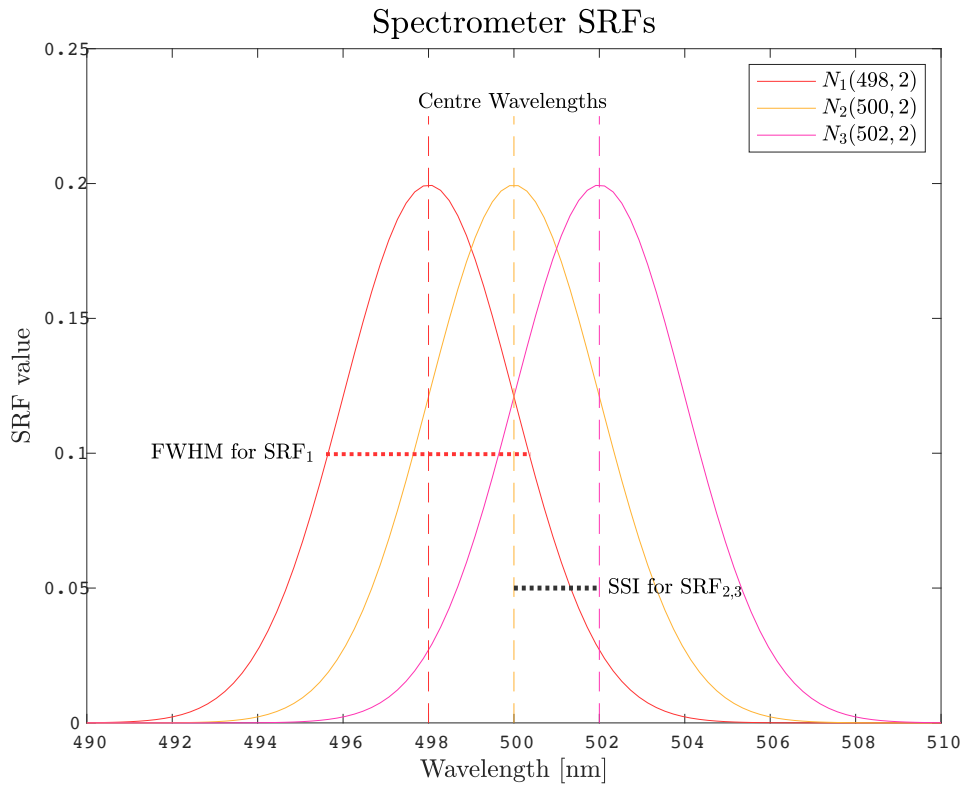

Figure 2: Spectral response function (SRF) with centre wavelength λ_0, Full Width at Half Maximum (FWHM) and spectral sampling interval (SSI) for three different wavelengths. The Gaussian probability distribution function implicitly gives a higher weight to the values closer to the centre wavelength.

radiation and is tuneable, so it can be used as filter system. The third way of determining the SRF is by assuming the instrument's responsivity as constant within each bandwidth. In this case the signals of adjacent image pixels are used as reference values.

The uncertainties associated with the SRF are relating to several groups of sources. The spectral measurement can be inaccurate concerning wavelength, bandwidth or noise. Changes in calibration might happen due to vibrations during the transport, changes of environmental variables like temperature or humidity, damage through high energy solar radiation or contamination of the films. A third source of uncertainty is mathematically given by the interpolation between wavelenghts. When integrating with the trapezius rule, the space between measurement points is treated as linear. Some interpolated points will be estimated as too high and some as too low. The more measurements (the better the spectral resolution of the laser) the more likely the random noise will be 'averaged' during the integration (see section 2.2.2). Therefore, the extent to which noise is reduced depends on the amount of measured values describing the SRF. This amount of wavelengths used for the reference measurements is critical for the question whether the shape of the SRF is described sufficiently. Additionally, the question remains if the chosen Gaussian is a good fit. However, the convolution itself has a smoothing function since the process reduces noise. Therefore, the uncertainty is reduced by the spectral convolution.

2.1.5 Radiative Transfer

Obtaining a reflectance factor

The measured quantity is radiance, but the quantity of interest is the reflectance or reflectance factor. For a field spectrometer the reflectance factor is the percentage of radiance per wavelength that is reflected by the surface compared to what could potentially be reflected by a perfect isotropic and lossless surface for given illumination and state of the atmosphere. For a lossless, ideal diffuse reflector the reflectance does not change with the observation angle. Therefore, the spectral irradiance of for a perfectly white, Lambertian reference surface is measured as $E = L_{ref}\pi\ [Wm^{-2}\ nm^{-1}]$. For any other surface the reflectance factor can be determined with the field spectrometer as in equation 9. For a field spectrometer the reflectance factor is of hemispherical-conical geometry since the instrument is placed only 1-2 meters above ground. Despite the actual geometric situation, the measured hemispherical-conical reflectance factor (HCRF) is often treated as HDRF. Namely, the reflectance factor is the ratio between the spectral radiance of a target and the spectral radiance of a reference panel that is assumed to be an ideal diffuse and lossless surface. $\omega_{\text{reference}}$ compensates for the fact that a real reference panel is never a totally ideal Lambertian and lossless surface.

$$HCRF = \frac{L_{\text{target}}}{L_{\text{reference}}} * \omega_{\text{reference}} \tag{9}$$

Radiative Transfer Model

Similar to the reflectance factor $HCRF$ obtained by a field spectrometer, the radiance measured by the imaging spectrometer is transformed by approximation into a reflectance factor. Only now, the quantity of interest is not the reflectance factor at the instrument level but on the surface level instead. Since there is an atmosphere between the sensor and the target a Radiative Transfer Model (RTM) is required. In remote sensing Radiative Transfer Codes (RTC) calculate the radiance as it passes the atmosphere. Input parameters are:

- Characteristics of the radiative source, describing how much irradiance could possibly arrive on the surface of the earth if there wasn't an atmosphere ($E_0, cos(\varphi)$).
- Reflection properties of the topology (BHR, DHR, BRDF), describing how the surface reflectance behaves for different illumination conditions.
- The state of the atmosphere (τ_{total}), determining how much of the exoatmospheric solar irradiance arrives at the surface and could potentially be reflected and how much of the reflected radiance 'makes it through' to the sensor.
- Geometry of the sensor's view angle ($cos(\theta_{il})$), determining how much of the directionally reflected radiance can actually be observed by the instrument.
- The wavelength range and resolution (VIS to SWIR $[0.4 - 2.5\ \mu m]$, SRF) of the sensor, defining in which range and at which resolution the reflected radiance will be measured.

The goal of a Radiative Transfer is to estimate the hemispherical-directional surface reflectance $\hat{\rho}_r$ in order to obtain an approximation for the hemispherical-directional reflectance factor (HDRF). The available data for the estimation is the calculated spectral reflectance at the sensor $\rho_{\text{instrument}}$ defined as in equation number **??**. L_{scene} represents the observed and calibrated spectral radiance at the sensor which is normalised by π and E_0 (the extraterrestrial solar irradiance) multiplied by $cos(\theta_0)$ (the cosine of the solar zenith angle). The observed upward radiance within the visible to shortwave infrared range consists of the following elements presented in figure 3.

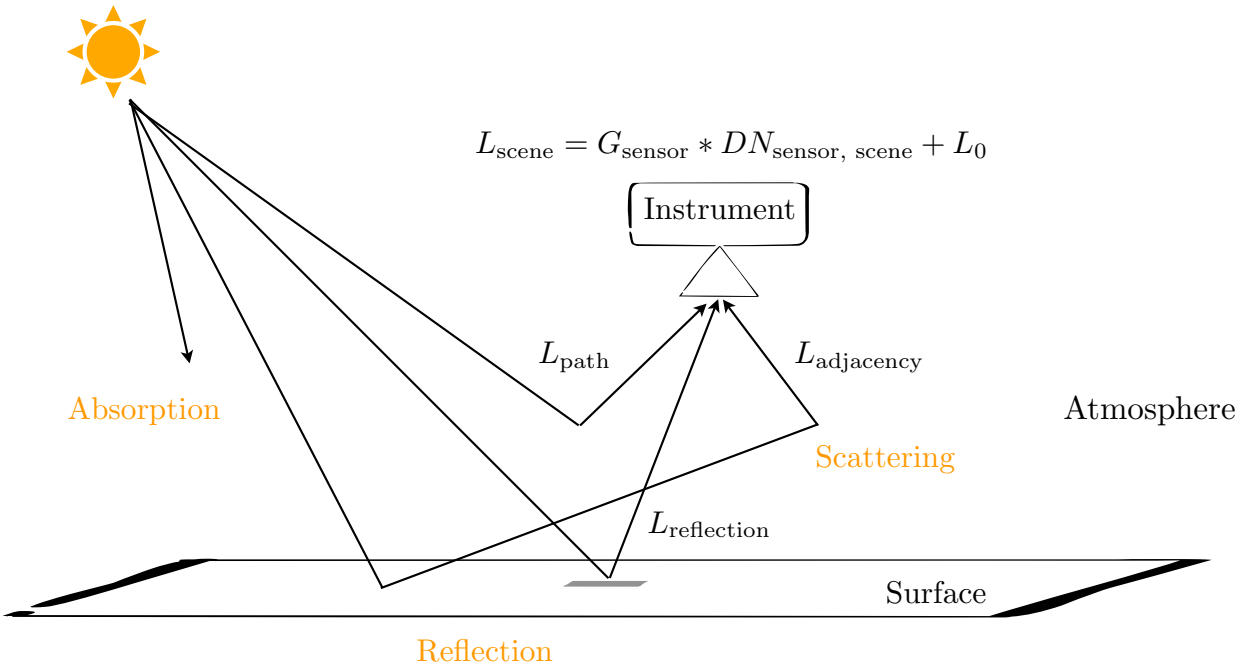

Figure 3: The path of the different components of the at-sensor radiance. The total radiance measured at the sensor consists of $L_{\text{reflection}}$, $L_{\text{adjacency}}$ and L_{path} (see equation 7a). Here, $L_{\text{reflection}}$ is the radiance reflected on the ground by a pixel with diffuse and direct irradiance, also referred to as L_g. The radiation reflected by the surrounding area of the pixel is represented by $L_{\text{adjacency}}$. The photons who scatter directly into the sensor and never 'touch the ground' are included as L_{path}.

$$L_{\text{scene}} = L_{\text{path}} + L_{\text{reflection}} + L_{\text{adjacency}} \tag{10}$$

- Photons reflected by the atmosphere and scattered into the sensor without reaching the surface are represented as L_{path} in Figure 3. The atmospheric path radiance is defined as $L_{\text{path}} = \frac{1}{\pi} E_0 \, \rho_{atm}$. The atmospheric reflectance ρ_{atm} is often referred to as spherical albedo of the atmosphere.
- Photons who were directly transmitted downward to the target, reflected and transmitted directly upward to the sensor are represented as $L_{\text{reflection}}$ in Figure 3. The direct ground reflected radiance is defined as $L_{\text{reflection}} = \frac{1}{\pi} E_g \, \rho_r \, \tau_{up}$. This is generally the value of interest.
- Photons scattered by the atmosphere before and/or after being reflected at the target's neighbouring surface and then being scattered into the sensor are summed as $L_{\text{adjacency}}$ in Figure 3. This term is defined as $L_{\text{adjacency}} = \frac{1}{\pi} E_g \, \rho_{adj} \, \tau_{up,\, adj}$. Hereby, E_g is the solar irradiance on ground as described in equation number 4c. ρ_{adj} is an average of the reflectance of the adjacent areas and $\tau_{up,\, adj}$ is the upward transmittance of the atmosphere above the adjacent area.

According to equation 5 the reflectance at the sensor is characterised as follows in expression 11a and 11b. In the first part equation 11a the reflectance at sensor is described as the ratio of the measured radiance to what

could be measured if the surface would be Lambertian. It is to mention that for airborne imagery E_0 for the upward transmittance should be E_f with f being the flight altitude. The second equation characterises the same value but with a different approach. The adjacency effect is neglected in equation 11b by the assumption that $L_{reflection} + L_{adjacency} = L_g$. In this second equation the at-sensor reflectance is described in terms of reflectance values instead of radiances which makes the value independent of solar illumination and angles.

$$\rho_{\text{scene}} = \frac{\pi \, L_{\text{scene}}}{\tau_{up} \, E_g} = \frac{\pi \, \left(L_{\text{reflection}} - L_{\text{adjacency}} - L_{\text{path}} \right)}{\tau_{up} \, \left[E_0 \, \tau_{down} \, cos(\varphi) + E_0 \, \tau_{down,\, dif} \, V_{sky} + E_{ter} \right]} \tag{11a}$$

$$\rho_{\text{scene}} = T_{gas} \left(\rho_{atm} + \frac{\tau_{down} \, \tau_{up} \, \rho_s}{1 - S \, \rho_s} \right) \tag{11b}$$

In expression number 11b the reflectance at sensor level ρ_{scene} is being described for a horizontal surface with reflectance $\rho_s = \rho_r + \rho_{adj}$ and spherical albedo of the surface S. The at-sensor reflectance is influenced on its path through the atmosphere by the transmittances τ_{down} downward the atmosphere from the sun to the surface and τ_{up} upward the atmosphere from the surface to the sensor. Those transmittances are mainly different due to diverse path lengths as the airborne sensor is not placed outside of the atmosphere. The radiances $L_{\text{reflection}}$ and $L_{\text{adjacency}}$ are summed in the term 'reflectance of the surface' L_s with reflectance ρ_s. Both, ρ_s normalised and ρ_{atm} need to be factorised by the gaseous absorption T_{gas}. The spectral resolution of gas absorption features is very high. The band resolution of the spectrometer might be to coarse. In this case it is typically necessary to re-sample the spectral resolution by the sensor's Spectral Response Function SRF (surveys in geophysics). Figure 4 shows how a variety of gases influences the transmittance of the atmosphere at different wavelengths.

To decouple T_{gas} from τ_{up} and τ_{down} might not be accurate for a real scene. The different transmittances can be summed in one variable. In equation number 12 the transmittance τ_{total} includes atmospheric gas absorption as well as atmospheric scattering. The path reflectance ρ_{atm} and the spherical albedo S can as well be reformulated with the gaseous absorption already included. The surface reflectance can now be estimated as follows in expression nr. 12. The HDRF can then be approximated as the fraction of the estimated surface reflectance to the surface reflection of a Lambertian target under the same conditions.

$$\hat{\rho}_s = \frac{1}{\tau_{total} \left(\rho_{scene} - \rho_{atm} \right)^{-1} + S} \tag{12}$$

2.1.6 Atmospheric Parameters

In order to estimate the surface reflectance accurately, the transmittance and absorption variables need to be determined with care. A variety of parameters determine the state of the atmosphere who's spatial and temporal changes can occur on a short scale. The following section is a summary of the most important state variables. For each variable follows the definition, the underlying assumptions, its influenced parameters in the RTM and a short summary of the standard retrieval procedures. The section is mainly based on the textbook 'Retrieval of Atmospheric Parameters and Surface Reflectance from Visible and Shortwave Infrared Imaging Spectroscopy Data' (Thompson et al., 2018).

Pressure Altitude: The pressure altitude is defined as the surface pressure photons are under along the sensor's optical path. This variable influences scattering and absorption mechanisms. Therefore, pressure altitude has

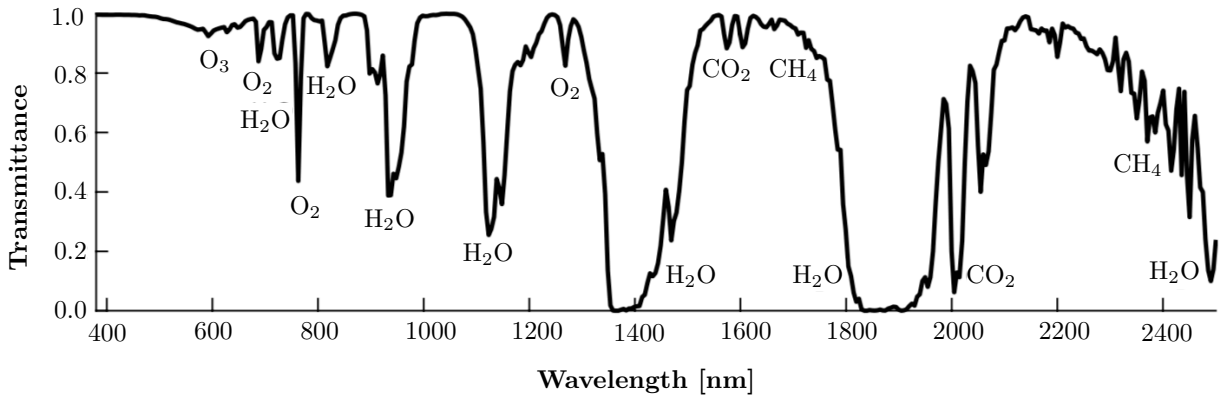

Figure 4: Gas absorption T_{gas} leads to a decreased transmittance of the atmosphere and strongly depends on the wavelength (Thompson et al., 2018).

an impact on the path radiance L_{path}, the gaseous absorption T_{gas} and the transmittance τ. Generally, the pressure altitude is a function of surface elevation under normal barometric conditions. The retrieval of the surface pressure is therefore often done with a DEM or by assuming one elevation for the whole scene (flat terrain). The standard procedure for estimating the state variable of the surface altitude is by continuum removal of the oxygen a band at ca 760 nm. In continuum removal the band depth for the absorption feature of oxygen a is calculated by linear interpolation between the neighbouring (non-affected) bands.

Water Vapour: The column water vapour is defined as the amount of absorption caused by H_2O molecules in the atmosphere. Water vapour has a strong spatial influence on the measured radiance. In the RTM, water vapour therefore needs to be included as a terrain dependent function of space. Typical absorption bands are at 820, 940 or 1130 nm. The common assumption for the retrieval of water vapour amount is the reflectance as a perfectly linear continuum. So, when looking at the band depth of a H_2O absorption feature (as in Figure 4) the interpolated line between left and right continuum interval is assumed as a linear function with a continuum slope of Δreflectance/Δwavelength. As an alternative the shape of the H_2O absorption features can be matched with spectral curve fitting for the full measurement spectrum. ATCOR however implements a different procedure with an atmospheric pre-correction. The RTC calculates L_{path} for a specific scene and atmospheric condition in order to find a conversion function between transmittance and water vapour.

Other gases: Other gases like ozone O_3, methane CH_4 or carbon dioxide CO_2 have absorption features in the VIS to SWIR range too. They as well influence the transmittance at a variety of wavelengths. The concentration of most of these gases is predictable. Typically, this information is retrieved from other sources than the measured spectrum. The gas concentration usually changes on a slower timescale (not within one recording) and is spatially homogeneous within a typically sized airborne scene. For example ozone changes on a monthly scale within 50 to 100 Dobson Units on a vertical spatial scale and within 100 to 500 km on a horizontal spatial scale. So, the concentration values can be obtained at a weather forecast agency and subsequently the transmittance can be calculated with a spectral absorption coefficient and knowledge of the solar and sensor view angle.

Aerosols and Haze: Aerosols and haze are suspensions of solid or liquid particles in the air. The amount of aerosols in the atmosphere can have a large impact on the visibility, the atmospheric scattering processes and

the transmittance in general. Since aerosols and haze are very heterogeneous, there are no clearly distinguishable absorption features in the reflectance spectra for this kind of variable. Instead, aerosols and haze induce spectrally smooth perturbations. The estimation of the aerosol amount is traditionally done by comparing reflectance spectra of the scene to reference surfaces. Often, the reference surface is a dark pixel for which the difference between the measured value and zero can is assumed to be the spectrally homogeneous aerosol and haze influence. More elaborated approaches take dark vegetation pixels as reference, since vegetation is less scene-dependent than random dark pixels. However, if there is no vegetation in the scene this method is useless as well. For water, the infrared channels can be used since water is practically absorbing the total infrared irradiance. And for a heterogeneous land-scene with good spatial resolution shadow pixels can be used as reference spectra. For the shadow-approach a radiative transfer model of the atmospheric compensation is used to compare the shadow areas to the directly illuminated pixels after inverting the measured radiance. Especially for haze, statistical methods are an efficient way to do a pre-processing by estimating the haze contribution in the reflectance spectrum of each pixel (because haze might be spatially heterogeneous within one image). However, none of these procedures is applicable for an investigation of the entire globe. With another radiative transfer approach where detailed surface models are used to create a lookup-table for different aerosol to surface combinations the application on a variety of surface types is possible. The method is a probabilistic approach. The strategy is to find the joint probability of surface type and aerosol combinations by including climatology and expected values as a prior.

2.1.7 The Process of Atmospheric Compensation

The past sections treated different aspects of the physical and technical quantities involved in the retrieval of surface reflectance through an imaging spectrometer. In the process of complete atmospheric correction the following steps are are carried out. To perform the atmospheric compensation specialised software as ATCOR, ATREM, FLAASH, or ACORN can be utilised. In the following example the ATCOR-4 (for airborne imagery) procedure is presented because this is the software used in the case study of this thesis. All of them use the radiative transfer code of MODTRAN in order to find a modelled HDRF by inversion of the reflectance at sensor level. The most important formula is equation 11a for the reflectance at sensor. Since most parameters in this formula vary for each pixel the calculation is based on look-up tables (LUT). Some atmospheric and radiative values are then taken from this LUT. Others are estimated during the process of the compensation trough the radiative transfer modelling.

1. Creation of a LUT with all necessary parameters than can or are not reasonable to get during the inversion process from the obtained reflectance spectra. A possible software to use is MODTRAN. The initial atmospheric parameters are obtained this way and serve as a first guess for the primary estimation of the surface reflectance retrieval.

2. Calculation of height and position for every pixel. Those values can be taken from a pre-prepared DEM and determine the angles of each pixel as in figure 1. The skyview factor V_{sky} (through the skyview angle β) and the incidence angle φ can then be calculated from the topographic data. With the incidence angle it is possible to estimate the total irradiance on the ground (as described in equation4c and as in step 6 % 8) and the elevation angle of the sun.

3. Preparation of the image data. This step includes geocoding and calibration (radiometric-, data- and spectral- calibration). A pre-classification might follow here in order to determine which part of the image is land, water, cloud or snow (...).

4. Selection of fixed parameters as the flight altitude and the aerosol model.

5. Derivation of atmospheric parameters from the image itself as water vapor with band 820, 940 or 1130 *nm* or aerosols and haze through shadow pixels. The input data for this estimation is topographic terrain data, calibrated image data, initially guessed atmospheric parameters from the LUT and the preclassified map (removing cloudy areas). The result is the retrieval of aerosol and optical depth wich is recqiured for the transmittance.

6. Irradiance calculation and subsequent creation of an irradiance map of the scene with the use of the prepared topographic data (without clouds and haze). The irradiance map can be used later for a BRDF correction.

7. Inversion of the LUT with equation 11a by interpolation for each parameter for each pixel. This is the initial surface reflectance estimation. This step will be repeated in form of an iteration process.

8. Iteration over steps 5) & 7)) in order to correct for adjacency effects with simulated diffuse ground irradiance. Likewise, shadow correction can be performed for cast, clouds and buildings by applying a separate compensation model.

9. Performance of the atmospheric compensation with equation 11a in order to find the hemispherical-directional reflectance factor $HDRF_{measured}$ for each pixel. This value describes the fraction of incident hemispherical light reflected into the FOV of the sensor.

10. Using a spectral database as a reference for a quantitative classification of the $HDRF_{measured}$ in order to determine the anisotropy factor K for each image pixel.

11. Eventual performance of a BRDF correction (with input irradiance map and K-map) for the BRDF correction in order to finally describe the reflectance properties of the surface (the spectral albedo BHR).

2.2 The principles of uncertainty analysis

The content of the following chapter is mainly based on the Training Course Textbook Intermediate Uncertainty Analysis for Earth Observation (Instrument Calibration) (2014) written by Emma Woolliams, Andreas Hueni and Javier Gorroño. This course was produced for the MetEOC (European Metrology for Earth Observation and Climate) project and funded by the European Metrology Research Programme.

2.2.1 Definitions and terminology

The error of a measurement is defined as the difference between the measured and the true value. The measured value is the result of a measurement process. Usually, in spectroscopic earth observation the surface measurements are done with a field spectroradiometer. For the case of airborne measurements a pushbroom imaging spectroradiometer is mainly used as a sensor. The true value is - and will always be - unknown. The difference between true and measured value can be split into a known and an unknown error. Known differences can be compensated for by mathematical corrections or -more accurately- compensations. These compensations can never be perfect, because they are based on physical models, assumptions and estimated parameters. On the other hand, there are effects that can not be corrected since they are part of the unknown difference. Since there is always an unknown error, the total error of a measurement result can never be known completely. However, the error can be described as a draw from the probability distribution function (pdf) for a large set of measured values. The uncertainty is hereby the deviation of the probability distribution function. So, the standard uncertainty is defined as the standard deviation of the probability distribution function. The absolute uncertainty has the same unit as the measurand of the measurement. The relative uncertainty which is common for radiometric calibrations is determined by the absolute uncertainty per quantity. No matter what kind of uncertainty, the pdf allows to link the unknown error on the measured value and its associated uncertainty.

2.2.2 Drawing the uncertainty from the probability distribution

When drawing the uncertainty associated with the measured value from a probability distribution function the unknown error gets described. As a first example, a measurement has random effects. When repeating the measurement - or experiment - a large number of times it is possible to find the average of the measured values μ. Due to the random errors (for example noise) each measured value is different but the mean value will eventually be robust to random errors as the number of trials n converges to infinity. The mean difference between the obtained value and the average is the standard uncertainty σ associated with the random effects. The uncertainty is identical for each measured value since the pdf is the same.

As a second example lets look at a measurement with a known systematic effect, an unknown systematic effect and additional random effects. When looking at systematic effects the error is the same for every measured value. It is possible for known systematic effects to make a prediction from one measurement's error about other measured values. An example would be a certain instrument error that is the same for ervery measurement. So, the pdf is again the same for each measured value but the uncertainty can not be determined by repeating the experiment. The Central Limit Theorem states that the arithmetic mean will be approximately normally distributed when the experiment is repeated a sufficiently large number of times. The CLT applies for independent random variables with defined expected value and variance each. If the measuring process is

made with a systematic bias (non-independent variables) the systematic effects will distort the average value. Since some systematic effects are known, the pdf can be compensated for these errors. However, the unknown systematic effects will remain in the statistics. If the mean value would be compensated for systematic effects and transformed into a standard normal distribution its difference to zero would represent the unknown systematic effects. In this manner the systematic effects themselves can theoretically be drawn from the pdf as well. But the mean of the standard normal distribution will only in theory not be at zero. Since the unknown systematic effect is - as the name says - not known, the transformation from the normal to the standard normal distribution will result in $\mu = 0$. For this reason the standard uncertainty drawn from a standard normal probability distribution can only describe the random effects.

The procedure of repeating measurements, finding μ and σ and determining the uncertainty for random effects is called an evaluation of uncertainty by statistical analysis of series of observation. Other types of uncertainty evaluation can be by using prior knowledge, by modeling or by using other experiments as estimates. In those procedures it might be possible to describe systematic as well as random effects (GUM). For spectroradiometric measurements the uncertainty evaluation is usually a mixture of several of these types.

2.2.3 The Law of Propagation of Uncertainties

The aim of an uncertainty evaluation is to find a final uncertainty which combines the uncertainty of all elements within the measurement and processing process. The procedure of an uncertainty analysis is to find parameters for each element by measuring, setting, calculating or controlling them. At the end, the uncertainties are added in quadrature. According to the GUM the Law of Propagation of Uncertainty is defined as follows in equation number 13:

$$u_c^2(y) = \sum_{i=1}^{n} c_i^2 \, u^2(x_i) + 2 \sum_{i=1}^{n-1} \sum_{j=i+1}^{n} c_i c_j u(x_i, x_j) \tag{13}$$

The formula applies for a measurement model of the form $Y = f(X_1, X_2, X_3, ...X_i)$. The squared standard uncertainty $u_c^2(y)$ is equal to the variance σ^2 of the pdf and associated with the measured value y. The variance is composed out of a comnination of the uncertainties associated with the different effects x_i. The parameter x for each effect i is the estimate of the quantity X_i and has an associated uncertainty $u(x_i)$. Each uncertainty associated with an estimated effect x_i has a so called sensitivity coefficient $c_i = \frac{\partial y}{\partial x_i}$. The sensitivity coefficient describes how much the input quantity X_i influences the measured value Y. The uncertainty associated with the calculated Y due the effect X_i is $u_{y::x_i} = \frac{\partial y}{\partial x_i} u(x_i)$. Sensitivity coefficients can be derived mathematically trough differentiation, numerically by a model or experimentally in the lab.

Adding the uncertainties and their sensitivity coefficients in quadrature allows a statistically robust analysis. With squaring it doesn't matter if the uncertainty is positive or negative. If there is no correlation associated to the various effects the formula can be reduced to the first part as in equations 13 or 14 respectively. Then, the squared standard uncertainty associated with the measured value y equals the sum of the squares of the standard uncertainties $u(x_i)$ associated with each individual effect multiplied by the according partial derivative.

$$u_c^2(y) = \sum_{i=1}^{n} c_i^2 \, u^2(x_i) = \sum \sigma^2 \tag{14}$$

For $n = N$ independently measured values the sensitivity coefficients can be assumed as $c_i = \frac{\partial y}{\partial x_i} = \frac{1}{N}$. When assuming independent measurements the uncertainty for each effect can be described as $u(x_i) = u(x)$. The uncertainty of the mean μ can then be described for the estimate x as $\left(\frac{u(x)}{\sqrt{N}}\right)^2$. So, for N independent measurements $\sum_{i=1}^{N} \left(\frac{1}{N}\right)^2 u^2(x_i) = N \left(\frac{1}{N}\right)^2 u^2(x)$.

In order to get robust sensitivity coefficients it is therefore necessary to have a good estimate for $u(x)$. Since σ is unreliable for a small N the number of measurements should be adequately high. Nevertheless, averaging more and more measured values doesn't necessarily reduce the uncertainty. As mentioned, systematic effects cannot be averaged out. Additionally, instruments are likely to drift over time. Noise can therefore be separated into white and drift noise. White noise is simple noise which can be averaged and will be less weighted for a higher N. The drift noise is defined as the instrument change over time and will -in comparison to white noise - get higher with an increasing N. If there is drift noise averaging will actually make it worse after a certain point in time. This point in time is called the Allan Deviation minimum and is calculated by the variance as a function of time $\sigma(\triangle t)$. Through the time series it is possible to determine whether and when it concerns white or drift (or any other kind of) noise. Other ideas to reduce the uncertainty in order to receive more reliable sensitivity coefficients for independent measurements are for example the inclusion of data from adjacent wavelengths (smoothing) or taking the values at the beginning of a measurement series as reference. The distinction of white and drift noise as well as the reduction of noise in general is not within the scope of this thesis. However, these topics are crucial for any uncertainty analysis and therefore the previous paragraph still got included.

As mentioned, the Law of Propagation of Uncertainties is devided into two parts. The second segment of equation number 13 is dedicated to non-independent measured values. If measured values have the same errors this is an indicator for systematic effects. In this case, the measured values correlate. Correlation appears between multiple measured values due to a common effect in the measurement process and can be modelled out. Analytically, absolute uncertainties associated with correlating measured values can be determined as in equation 15. Hereby, Y_i represents the measured value obtained by a measurement. Y_T is defined as the unknown true value. R_i stands for the random error of the ith measurement drawn from the pdf with uncertainty $u(R)$ associated with random effects. S is the systematic error in all measurements and comes with an uncertainty of $u(S)$ associated with systematic effects.

$$Y_i = Y_T + R_i + S \tag{15}$$

$$u^2\left(Y_M\right) = \left(\frac{u(R)^2}{\sqrt{N}}\right)^2 + u^2(S) \tag{16}$$

Equation number 16 describes the uncertainty associated with the mean (μ) of the measured values Y as Y_M for a set of N measurements. As for independently measured values, the sensitivity coefficient for the random error is $\frac{1}{N}$ and the uncertainty $u(R_i)$ equals $u(R)$ what changes compared to the independent case is the addition of the uncertainty associated with systematic effects $u(S)$. Since the systematic effects don't change between measurements, the uncertainty $u^2(S)$ remains unchanged by averaging and can be calculated as the quadrature sum of the individual uncertainties. Again, the uncertainty associated with systematic effects is added in quadrature. For this addiditve model the relative uncertainties behave exactly like the absolute uncertainties. Assuming $u(R_i) = u(R) = 0$ the uncertainty per measurement can be modelled analogous to the

absolute uncertainty of equation 16.

Another method of deriving absolute uncertainties for correlating measured values is by calculating the covariance $cov(X_i, X_j)$ for pairs of measuered values (i, j). This answers the question of how much each pair of quantities varies together. The shared variety comes from systematic effects. Therefore, the covariance or uncertainty $u(X_i, X_j)$ is equal to the uncertainty associated with systematic effects $u^2(S)$. According to this definition, the uncertainty of the mean of the measured values $u^2(Y_M)$ can be determined as in equation number 16.

Before, in equation 16, the modelled uncertainty associated with systematic effects was added to the modelled uncertainty associated with random effects. In equation 13 about the Law of Propagation of Uncertainty the covariance of the correlated quantities is added to the uncertainty associated with independently measured values in an analogous way. Hereby, $i < j$ since $cov(x_1, x_2) = cov(x_2, x_1)$ and the sum of the covariances is multiplied by 2 instead. If the covariance is estimated from experimental data (instead of modelled) the uncertainty is calculated statistically as $u(x_i, x_j) = u(x_i)u(x_j)r(x_i, x_j)$. The correlation coefficient $r(x_i, x_j)$ for n number of data pairs (X_i, X_j) lies between -1 and 1. While $r(x_i, x_j) = 0$ represents entirely uncorrelated data, $r(x_i, x_j) = 1$ or $r(x_i, x_j = -1$ describe entirely correlated data. Within the range of 0 to 1 the uncertainty increases compared to uncorrelated data. This is the case if the sensitivity coefficients have the same signs. If they have opposite signs the correlation coefficient will be in the range of 0 to -1 and the uncertainty increases. A negative covariance occurs when the uncertainty associated with one systematic effect is compensated through the uncertainty of an other effect. The errors are 'cancelled out' in this scenario and the uncertainty decreases.

2.3 The uncertainties associated with atmospheric compensation

Generally, the aim of atmospheric compensation is to find a method with low uncertainty and at the same time applicability all over the globe. This is especially important for spaceborne sensors which cover the surface of the entire earth, but it is relevant for airborne imagery as well. The goal is to find a method which can be used for every scene in order to make different measurements comparable. Until now, atmospheric compensation approaches perform usually well for a specific scene which is very often a place where ground measurements can be taken as well. But for many regions in the world, ground measurements can not be taken easily. These are typically underrepresented study objects. In a scene with clear sky and a nadir-looking sensor it is ususlaly possible to perform an accurate atmospheric compensation. But for examples in a scene of tropical forest where the atmospheric conditions change relatively fast and a lot of haze and water is in the air, the standard algorithms perform much less accurate.

Until now, the presented uncertainties that can occur during imaging processing are associated with the solar irradiance reference spectrum, the calibration of the instruments, the calibration of the data, spectral convolution, assumptions as the one of a Lambertian surface and unclearly defined parameters. Especially the last one is very interesting when talking about the atmospheric compensation. The so called reflectance at surface - the result of an atmospheric compensation process - is not a clearly defined term. The illumination conditions and the type of reflection should be indicated in the term. For this reason, many studies and software use the term HDRF. With 'hemispherical' illumination and 'directional' reflection this term is more clearly defined. However, the measured HDRF consists of two parts, the directional reflection for direct illumination and the directional illumination for diffuse illumination. This second part is again called HDRF. Therefore, the result of the atmospheric compendation sould be named 'measured HDRF'. Additionally, the measured HDRF should actually be called a measured HCRF due to the angular sensitivity of spectroscopic measurements. If the sensor captures a relatively big fragment of the surface, the assumption of a zero interval for the solid angle of the reflected radiance (completely directional) is not true. Since airborne sensors have a FOV of ca. 0.03 degrees the validity of the just mentioned assumption is not violated. But in field spectroscopy the assumption of a purely directional measurement is never true since the spectrometer has a relatively large FOV of around 20 degrees (Hueni et al., 2016).

For airborne data - no matter if HDRF or HCRF - the result of the atmoshperic correction is a description of reflectance properties of the surface under examination. For field spectroscopy, the result is a reflectance factor. So, when comparing those two values for a simultaneous point of aquisition, the measured reflectance factor is the relative description of the surface reflection at this moment and the measured HDRF could be seen as an absolute value (or rather a description). Those two values can therefore not per se be compared. In combination they might describe the current surface properties very well, but the field measurement can not directly be taken as a reference for uncertainty calculations.

Alternatives to the radiative transfer based method of atmospheric compensation are: "empirical approaches like scene averaging (Kruse 1988), flat fielding (Roberts et al. 1986), quick atmospheric correction (QUAC, Bernstein et al. 2005), and cloud shadow methods (Reinersman et al. 1998)" (as cited in: Thompson et al., 2018a). For all of these methods and the RTM based approaches as well the uncertainty analysis can only be done after the process in retrospect. This is unfortunate in terms of accuracy since the performing algorithms often can not be evaluated by themselves. The only method is to compare the results of the algorithms and validate them in relation to the - only partly comparatible - reference measurements.

In Thompson et al. (2018b) use a combination of ground and atmospheric state variables as input to a new form of atmopsheric compensation based on optimal estimation (Rodgers, 2000). In this approach the ground reference data gets included into the atmospheric compensation process as part of a joint probabilitsic variable. Based on the joint probability of the field measurements and the atmospheric parameters derived from MODTRAN the reflectance estimation can be done in an approximation process. Compared to ATCOR-4, the uncertainty can hereby be reduced since the atmopsheric parameters derived from MODTRAN are set in relation to the actual conditions measured on the ground. In this manner it is possible to revieve a uncertainty value for the product within the process of the compensation.

In the following study the aim is to find the uncertainty associated with a variety of input paramaters for the atmospheric compensation in ATCOR-4. By tracking down what happens for different aspects while run through the atmopsheric compensation algorithm, it might be possible to get a clearer image of how the total uncertainty $u_c^2(y)$ comes about. The conclusive value for the combined standard uncertainty can not be found within the scope of this thesis. The focus lays on a set of parameters that are mainly independent from each other so that systematic effects theoretically should take a secondary role.

3 Case Study in Wettingen

3.1 Data

The data used in the case study consists of airborne data from two different sensors (APEX and AVIRIS NG) and field measurements taken by a field spectrometer. The software used for the data analysis were MODO and ATCOR-4. Both use the ratiative transfer codes of MODTRAN.

3.1.1 Reference Measurements by Field Spectrometer and the Study Site

The measurements taken by a high-resolution field spectrometer were obtained with an ASD FieldSpec Pro (Panalytics, CO, USA) measurement device. The ASD spectrometer measures at a wavelength range of 350 to 2500 nm. The bandwidth for bands below 100 nm is 3 nm, for higher bands it is 10 nm (Hueni et al., 2016). The instrument's field of view is 25°.

The measurements were taken at approximately the same time as the airborne sensors were measuring from above. The acquisition date was on the 9th of July in 2018 at about 12 o'clock am. The surface types measured and later used as reference spectra were two different soccer fields, two different types of sand, asphalt, water and blue as well as red tartan ground. All those measured surfaces are spread over the town of Wettingen in Switzerland, in the canton of Aarau. The study area is right to the Laegern forest which is as well part of this airborne campaign as the flight stripes include large parts of the forest too. However, the field data used in this thesis was taken in an urban area. Therefore, artificial surface types are highly represented among the data points.

For example blue and red tartan show reflectance spectra that aren't typically found in nature. However, these surfaces provide a valid data set for the task of the validation of the airborne measurements since they are very distinctive. The water data was taken in an environement close to a bridge. Therefore, there might be some shadow effects or high adjacancy reflectance for this reference spectrum. The same applies for the dark sand which is actually a rather small area of sand. Additionally, the data points of bright sand and one of the soccer fields lay at the edge of the APEX image flight stripe over Wettingen. Therefore, when doing a comparison of airborne and ground measurement, it is possible that the algorithm of the atmospheric compensation didn't compansate as well for the adjacency effect outside the image compared to what influences the ground maeasurement for this area.

In general, the study site Wettingen (47°28'18"N, 8°19'32"E) is an urban area in the midlands of Switzerland with an average elevation of 570 meters above sea level. Some agricultural fields can be found towards the Laegern. The river Aare is seperating the own into two parts and provides the data set with water pixels and shadow pixels from the adjacent trees and bushes next to the river. Within the city the area is flat and towards the forest the slopes and elevations become a bit higher. In figrue 5 there is an image of the area from maps.admin.ch with the two airborne campaings marked as well as the area in which the reference spectra were derived.

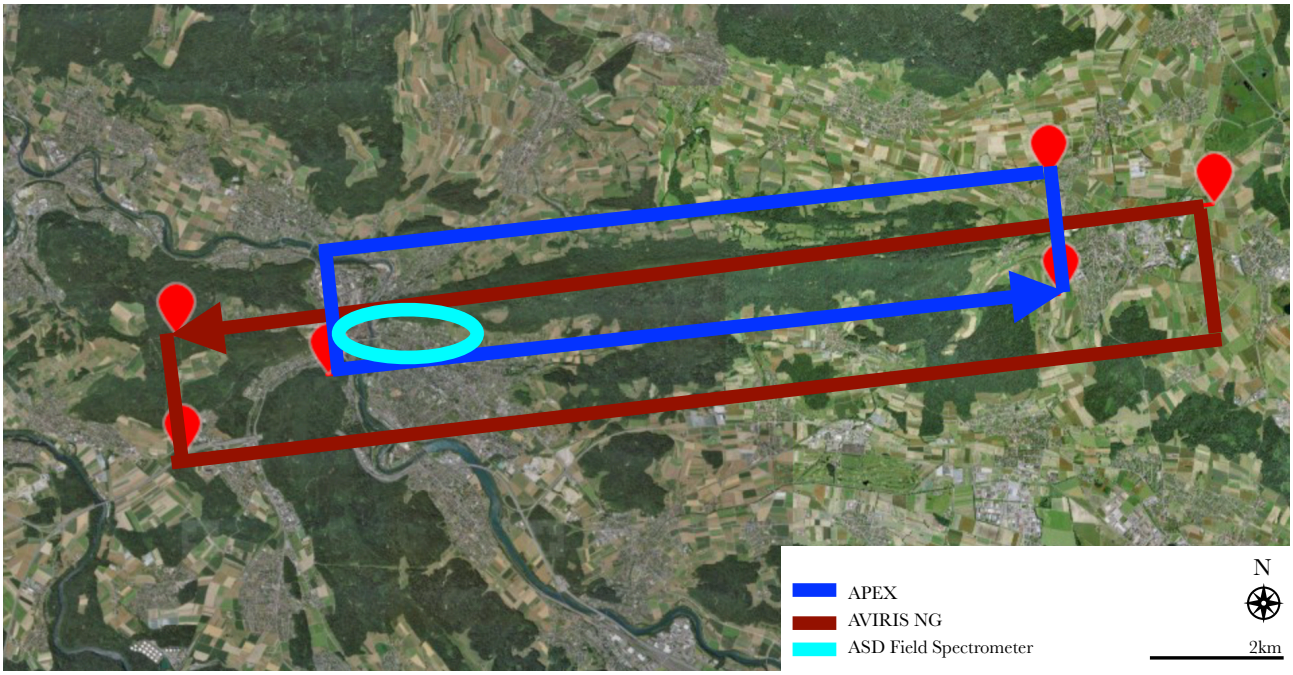

Figure 5: The test sity Wettingen with Laegern and the flight paths of AVIRIS NG and APEX included. APEX is blue and AVIRIRS NG is represented as red. The arrows indicate the flight direction. Source of image: www.maps.admin.ch.

3.1.2 Airborne Data

The APEX (Airborne Prism Experiment) data was derived by a pushbroom imaging spectrometer with a single flight on July 9th in 2018. The acquisition time was 11,57 to 12,00 am. The Cessna airplane had a height of flight of 4.144 km and the mean ground elevation within the image is 594 meters above sea level. The resulting image consists of 6364 pixels along track which corresponds to about 13 km. The pushbroom imaging spectrometer is built up from of 1000 across track pixels with each pixel covering an area of size 2.05 meters. The solar zenith angle was taken as 25.7 degrees and the solar azimuth angle as 194.2 degrees. The channels of this spectrometer are positioned at the visible to near-infrared as well as in the shortwave infrared wavelengths. The two sensors are spectrally overlapping at near-infrared since the VNIR channels cover 372 to 1015 nm and the SWIR channels cover 940 to 2540 nm.

The data from Next Generation Airborne Visible to Infrared Imaging Spectrometer (AVIRIS-NG) was as well acquired on the 9th of July 2018 bewteen 11,54 to 11,59 am. The solar zenith angle was taken as 25.5 degrees and the solar azimuth angle was estimated as 192.1. The overflown area was 15.5 km long. One pixel has a size of 2.9 meters. The flight altitude was 3.5 km above ground and the mean ground elevation over the entire image is 507 meters above sealevel. The reason for this lower value compared to APEX is that AVIRIS NG covered more of the urban and agricultural areas next to the elevated Laegern.

3.2 Software

The MODO software by ReSe is a graphical user interface for radiative transfer simulations in MODTRAN. The software runs on IDL. In this case study version 5.2.0 was used. MODO can be used to run MODTRAN, plot outputs of MODTRAN and extract spectra from those outputs. The data can be - depending on the tool - radiance values, transmittance values or reflectance estimates for either at sensor height or the surface level. The main applications in the case study were to calculate the changes in radiance for different solar zenith and azimuth angles, simulate parameter series like the solar reference spectrum or visibility and to simulate reflectence or radiance values for a given set of atmospheric state variables.

The data conversion and creation of subsets for the APEX and AVIRIS NG images was done in ENVI classic version 5.5.2 by Harris Geospatial Solutions. Different radiance intensities were produced with the Spectral Math tool of ENVI and for the extraction of spectral libraries the imaging tool was utilized.

ATCOR-4 version 7.3.0 by ReSe was used for the atmospheric compensation and the extraction of the resulting spectra. The airborne atmospheric compensation was done with and without digital elevation file which is the so called flat respectively rugged terrain mode in ATCOR-4. The sensor parameters for APEX were taken from the calibration files of $APEX/_2017/_high/_osu/_p$. For AVIRIS NG the default file of ATCOR-4 was used. Besides the atmospheric compensation, the tool for solar azimuth and zenith angle calculation was used in order to calculate them from the input parameteres of exact time and place.

The reference spectra from the ASD field spectrometer were stored and organised in the spectral database SPECCHIO. From there the reflectance values were extracted in order to compare them to the estimated HDRF values. For each reference spectrum acquisition point an image of the skyview, a description of the location, the exact geographic coordinates and a description of the measurement procedure can be found in SPECCHIO.

3.3 Method

The method for the simulation of different radiance intensities as input for the atmospheric compensation can be described as follows: In ENVI the original image with calibrated radiance values of the scene was modified by multiplying the radiance values with a variety of factors derived from a normal distribution around 100%. These are 0.5, 0.75, 0.9, 0.95, 0.99, 0.995, 0.999, 1.001, 1.005, 1.01, 1.05, 1.1, 1.25 and 1.5. In figure 12 and 17 those factors are referred to as 'f0500', 'f0750', 'f0900', 'f0950', 'f0990', 'f0995', 'f0999', 'f1001', 'f1005', 'f1010', 'f1050', 'f1100', 'f1250', 'f1500' and the original image is represented as 'f1000'. The multiplication had to be done on the radiance values, since the sensor (and its calibration) is supposed to be the same for all factors.

As a next step, the new images went through the atmospheric compensation in ATCOR-4. The AVIRIS NG radiances were all processed by flat terrain ATCOR with an adjacency of 600 meters, a visibility of 50 km, a solar azimuth angle of 192.1° and a solar zenith angle of 25.5°. The water vapor retrieval was chosen with band regression in the 940 nm region. All the APEX radiances for each factor were processed with rugged terrain ATCOR, visibility of 50 km and adjacency of 600 meters. Additionally, the HDRF of the original APEX image was estimated with zero meters adjaceny range and with ATCOR flat terrain for 600 meters adjacency. The comparisons can therefore be made between different factors, between APEX and AVIRIS NG for the original images and flat terrain, between APEX flat and rugged terrain for the original image and for the adjaceny effect in the original APEX image. An additional comparison is done for two different steps of the atmospheric compensation. The 'before' step refers to a moment in the procedure where the first estimation of irradiance was done and the atmospheric parameters were looked up in the LUT, but the iteration hasn't happened yet. Under section 2.1.7 this step is referred to in number 7. The adjacaency effect is then included for the 'after' image which corresponds to steps 8 and 9.

The calculation of the uncertainty was done according to the theory section based on the Training Course Textbook Intermediate Uncertainty Analysis for Earth Observation (Woolliams, Hueni and Gorroño, 2014) while assuming the wavelengths to be independent from each other. The resulting HDRFs for the different radiance factors were taken as input data for a ttest per wavelength. The resulting sigma could then be taken as the uncertainty per wavelength and was plottet for each reference data point as uncertainty associated with the HDRF. In a second calculation the variance of the pdf for the HDRFs with different factors was drawn in order to recieve the standard uncertainty associated with the variation due to different radiant intensities (see equations 14 to 16). For the second approach a normal distribution was assumed. The reflectance of the ground control points and the uncertainty associated with it were taken from SPECCHIO.

4 Results

4.1 Simulations and Models

4.1.1 Solar irradiance reference spectra

Referring to figure 6 it becomes clear that mainly in the visible to near infrared the two solar reference spectra show significant discrepancies. In figure 7 the difference between the solar reference spectrum of Fontenla (2011) and Thuillier (2002) is plotted per wavelength. The source of the irradiance data is MODTRAN. In absolute terms the differences between the two spectra is approximately within -0.05 to 0.04 $W/m^2/sr/nm$. However, in relative terms this is especially in the very short wavelength areas a difference of nearly 100%. As presented in figure 7 the relative difference is as high as 20% even at increasing wavelengths. In particular at 0.9 um can be observed an other range with larger differences. This band area is especially relevant since it is often used for the atmospheric water retrieval. The choice of reference spectrum can therefore not be ignored in an uncertainty analysis. Since it is difficult to draw a pdf from two measured values the uncertainty associated with the reference solar spectrum is rather included in the total uncertainty as a notion of significance for the consistency of choice. Since the reflectance values obtained by atmospheric compensation are all relative, the main importance is to stick to the choice of solar reference spectrum within one processing chain. This includes further processing steps after retrieving the HDRF or BDRF.

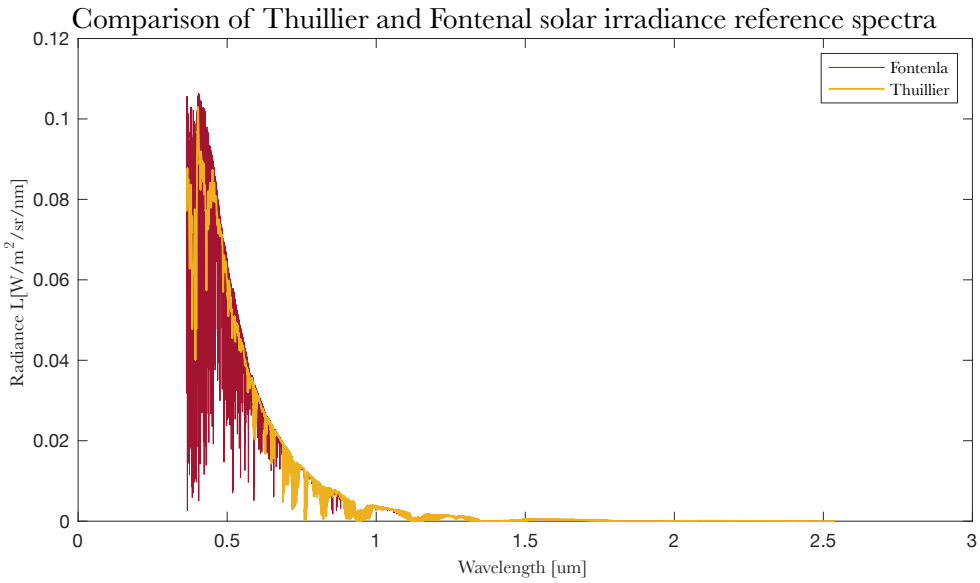

Figure 6: Comparison of two standard solar reference irradiance spectra ((Thuillier et al., 2002) and (Fontenla et al., 2011)) produced in Modo5.

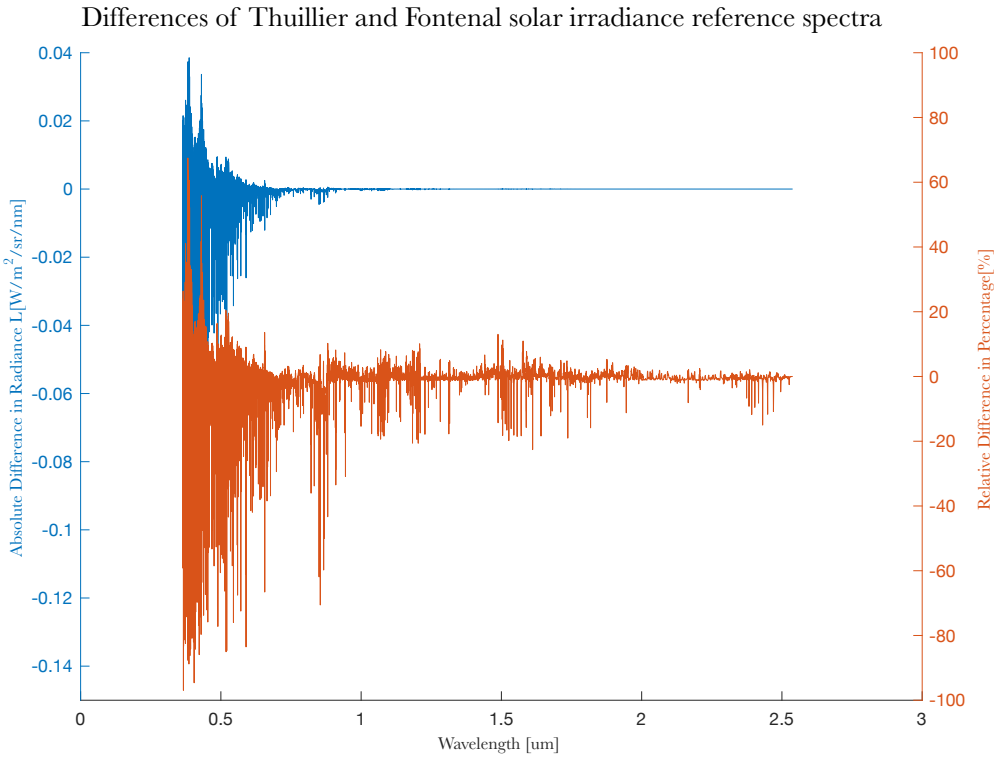

Figure 7: Illustration of the differnece between two standard solar reference irradiance spectra ((Thuillier et al., 2002) and (Fontenla et al., 2011)) produced in Modo5.

4.1.2 Solar angles during flight time

The solar zenith and azimuth angles for APEX are 25.7° and 194.2°. For AVIRIS NG these input values for the atmospheric compensation are estimated as 25.5° and 192.1° since this sensor's flight has a different flight line. However, when looking at the start and end date in UTC time for APEX as well as AVIRIS NG these two angles have a slightly different value. For the start values of APEX the solar azimuth and zenith angle in ATCOR-4 calculates a zenith of ... and azimuth of ... The angles on the end of the campaign are ... zenith and ... azimuth. For AVIRIS NG these values are ... and ... for the start and ... and .. for the end of the flight. The start and end coordinates do not only differ in along-track dimension but were as well calculated with respect to the across-track divergence. SO the start angles are calculated for pixel (1/1) and the angles of the end pixel represent the last pixel observed for this scene.

To answer the question of how those 0.2° might influence the irradiance estimated for the ground the for pairs of azimuth and zenith angles had to be simulated in Modo5. The result is displayed for APEX as well as AVIRIS NG in an absolute and relative difference plot. As observable in figure 8 and 9 the uncertainty associated with the solar azimuth and zenith angle chosen as input parameters for the atmospheric compensation is wavelength dependent. The absolute differences appear to get smaller with increasing wavelenghth. For both sensors the absolute radiance values vary within a range of 0.00004 $W/m^2/sr/nm$. This data was calculated as spectral radiance for end minus start date and point. Ignoring individual extrema, two local maxima of relative difference can be observed at 1.4 um and 1.9 um for both, APEX and AVIRIS NG. The overall relative difference vary for both sensors mainly within 0 to 2%. The differences are positive, since the start dates are

both a few minutes before 12 am, so the ground irradiance should still increase in the following minutes during the flight.

Again, for an absolute uncertainty value associated with variation of ground irradiance intensity during the flight time due to changing solar azimuth and zenith angle two sensors with one campaign each are not enough data. But similar to the solar irradiance spectra it is again important to state the significance of consistency. Further processing steps of the resulting HDRF data must include the solar zenith and azimuth values used in the atmospheric compensation. Additionally, it would actually be more accurate for the following comparison of the sensors to ground reference measurements, if the exact solar azimuth and zenith angle would be taken for each point of reference measurement. For longer flight campaigns it is definitely worth considering a time-dependent input ground irradiance for the atmoshperic compensation.

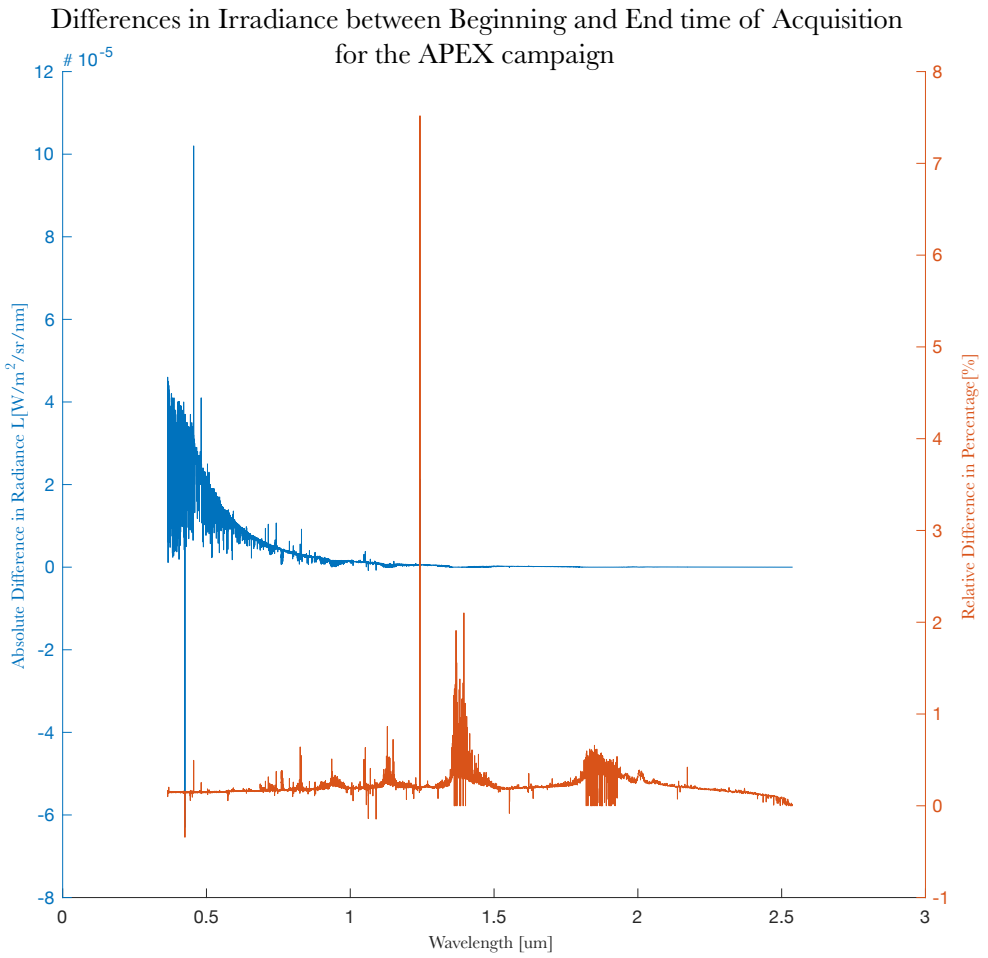

Figure 8: Illustration of the differences per wavelength in irradiance for the beginning and end time of acquisition produced in Modo5. The campaign is APEX for the 9th of July 2018 which is the 190th day of the year. The solar zenith angle changes within the flight time from 25.3° to 25.5°. The solar azimuth angle changes respectively from 192.0° to 194.4°. Theses values were taken specifically for start and end points on the ground of the campaign.

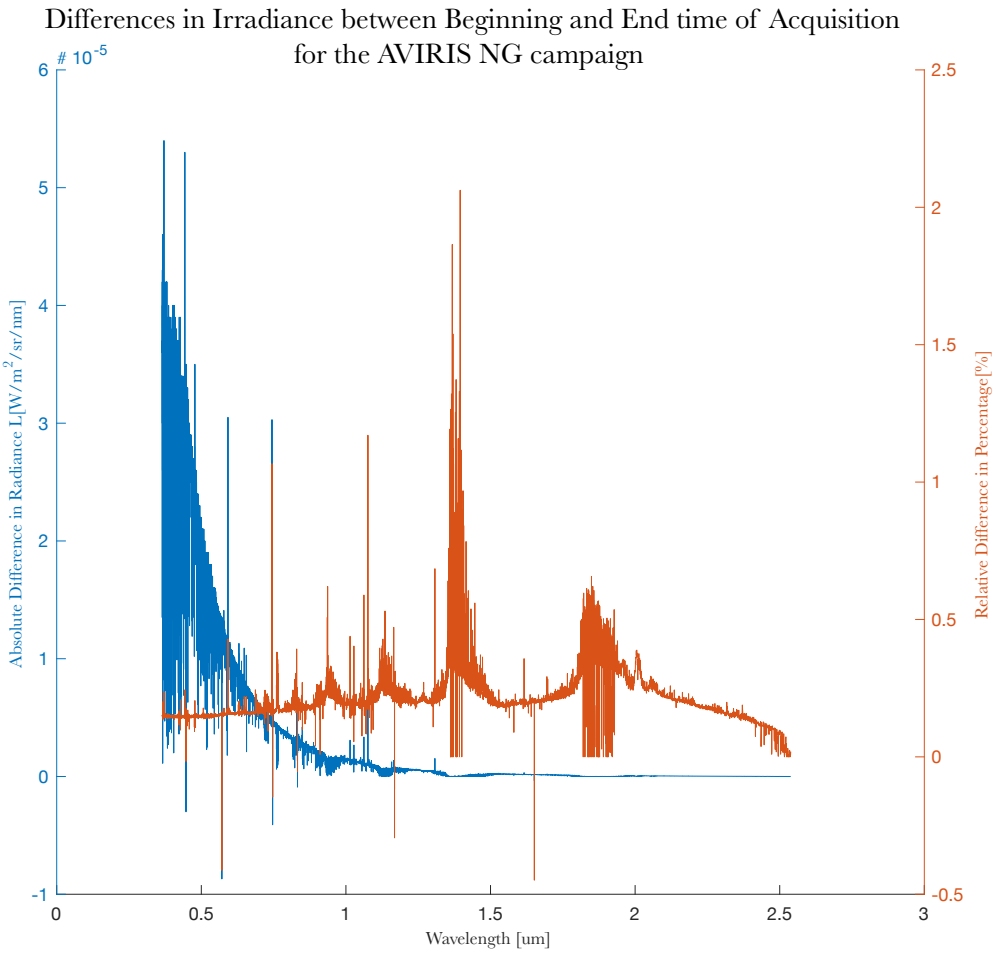

Figure 9: Differences per wavelength in irradiance for the beginning and end time of acquisition produced in Modo5. The campaign is AVIRIS NG for the 9th of July 2018 which is the 190th day of the year. The solar zenith angle changes within the flight time from 25.4° to 25.6°. The solar azimuth angle changes respectively from 193.4° to 195.1°. Theses values were taken specifically for start and end points on the ground of the campaign.

4.1.3 FWHM for APEX

Figure 10 shows the estimated mean per wavelength among all reflectance values produced with different input radiant intensity in ATCOR-4. Additionally, the full width half maximum values for each APEX band is plotted for each one of the eight reference field measurement points. The surface points could be any pixels for this figure. The main statement of this illustration is how the seemingly continuous reflectance spectra are actually merely interpolated estimations. At ca 0.95 um the FWHM ranges become appruptly wider than at lower wavelengths. So, the APEX instrument must be built out of two different sensors. Since the band accuracy for the sensor in the VIS to NIR range appears to be higher, the variation in the radiance and reflectance spectra in this area has a lower uncertainty associated with the sensor accuracy. This means, vor APEX bands in the VIS to NIR range the obtained radiances were measured at the centre wavelength with a higher probability than for the SWIR bands. In this analysis the FWHM values get treated like standard deviations.

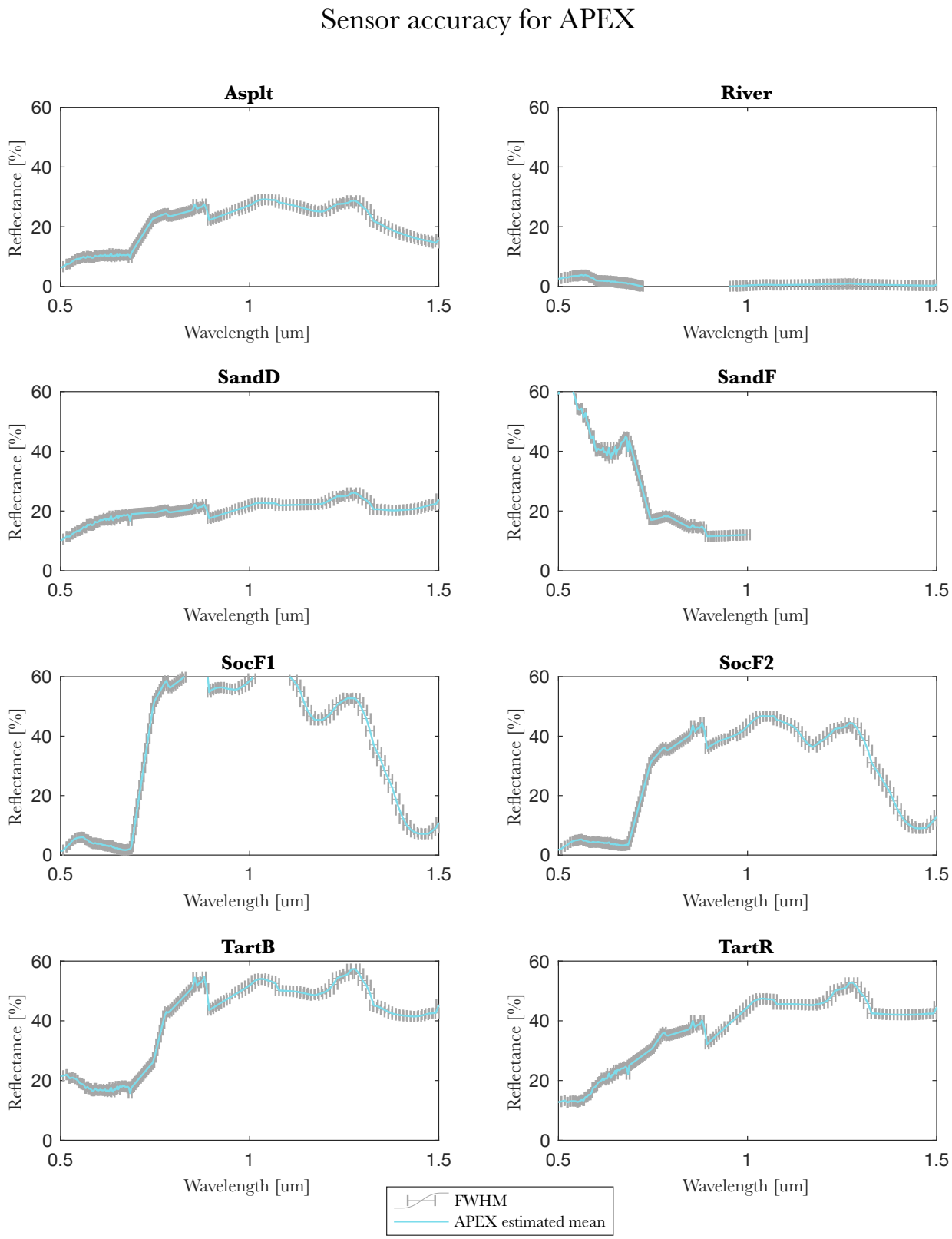

Figure 10: Full width half maximum plotted on the estimated mean APEX HDRF per surface type. The APEX sensor is

4.2 Reflectance values obtained through ATCOR-4

4.2.1 Influence of radiance intensity as input to ATCOR-4

Figure 11 shows the simulated radiance intensities for the reference surface types asphalt ('Asplt'), river ('River'), dark sand ('SandD'), fine sand ('SandF'), soccer field one and two ('SocF1', 'SocF2'), blue tartan ('TartB') and red tartan ('TartR') plus an additional vegetation point ('addPt') for a variety of factors. The added point has no ground reference data. All of the surface types have distinctive absorption features and they all have higher radiance values around 600 nm except for soccer field two and both tartan surfaces who have their maximum at 800 nm. These spectra still include atmospheric scattering since they haven't been compensated for atmospheric effects yet.

In figure 12 the estimated HDRF per wavelength per radiance factor per reference data point is presented. As expected, vegetation surfaces show higher reflectance factor values in the visible and near infrared area than artificial surface types. The river pixel has genrally a very low reflectance factor in every band with slightly higher responses in the short wave visible range. However, the fine sand sample spectra show some distinctive patterns in this area compared to the dark sand. For higher radiance intensities the resulting HDRF show higher absolute differences for different factors at the same wavelength. This is given due to multiplication of one reference spectrum. Threfore, the lower intensity radiance input spectra result in more homogeneous reflectance spectra compared to the specrta multiplied with higher factors.

In figure 14 the standard uncertainty is presented for the above reference data points. The differnet surface types have different uncertainty spectra. For example the river sample shows higher uncertainties towards samll wavelengths whereas asphalt, socer fields and tartan have higher standard uncertainty values around 1000 nm. The two samples of sand are very unalike as well. While the dark sand's uncertainty is relatively constant at 0.05% reflectance fine sand has much higher values around 0.15 in the range of 500 to 750 nm. Interestingly this pattern looks similar to the river uncertainty spectrum, but there the values lay between 0.005 and 0.01% reflectance. Soccer field onw and blue tartan are in the same range as fine sand with maximum uncertainty values above 0.1%. Soccer fiels two and red tartan have their maxima a bit lower at about 0.1% and dark sand and asphalt have thier maxima at 0.06%. The relative uncertainties mainly follow the pattern of the absolute uncertainties. However, the relative uncertainty of the surface types soccer field one and river is inverse to the standard uncertainty. Where the absolute uncertainty is high, the relative uncertainty is low.

Figure 13 displays how the values per band and surface type change over radiance intensity factors. As expected, the HDRF values are generally on a linear scale per band. The steepness of the linear function is increasing for higher reflectance values. Some anomalies however can be observed for a variety of the chosen reference pixels. For all of the surface types the values for the band around ca 620 nm and higher show a different gradient than the values of bands just below. For blue tartan, the soccer fields and fine sand this effect is especially well visible. The first assumption would be that those bands are part of an absorption feature and therefore have lower reflectance values and a lower slope when looking at the linearity of the factors. But for example for blue tartan the higher band values actually have a lower HDRF at 100% radiance and a higher reflectance at 50% radiance. So, this effect must have a different source. Another irregularity can be observed for the water surface. There, the negative values should theoretically multiply into more negative values. However, at about 95% input radiance the HDRF values start to increase. The values above zero reflectance and below 620 nm show the same break in linearity. Since water is the only surface type with this effect, this must

be caused by some sort of classification within the atmopsheric compensation process.

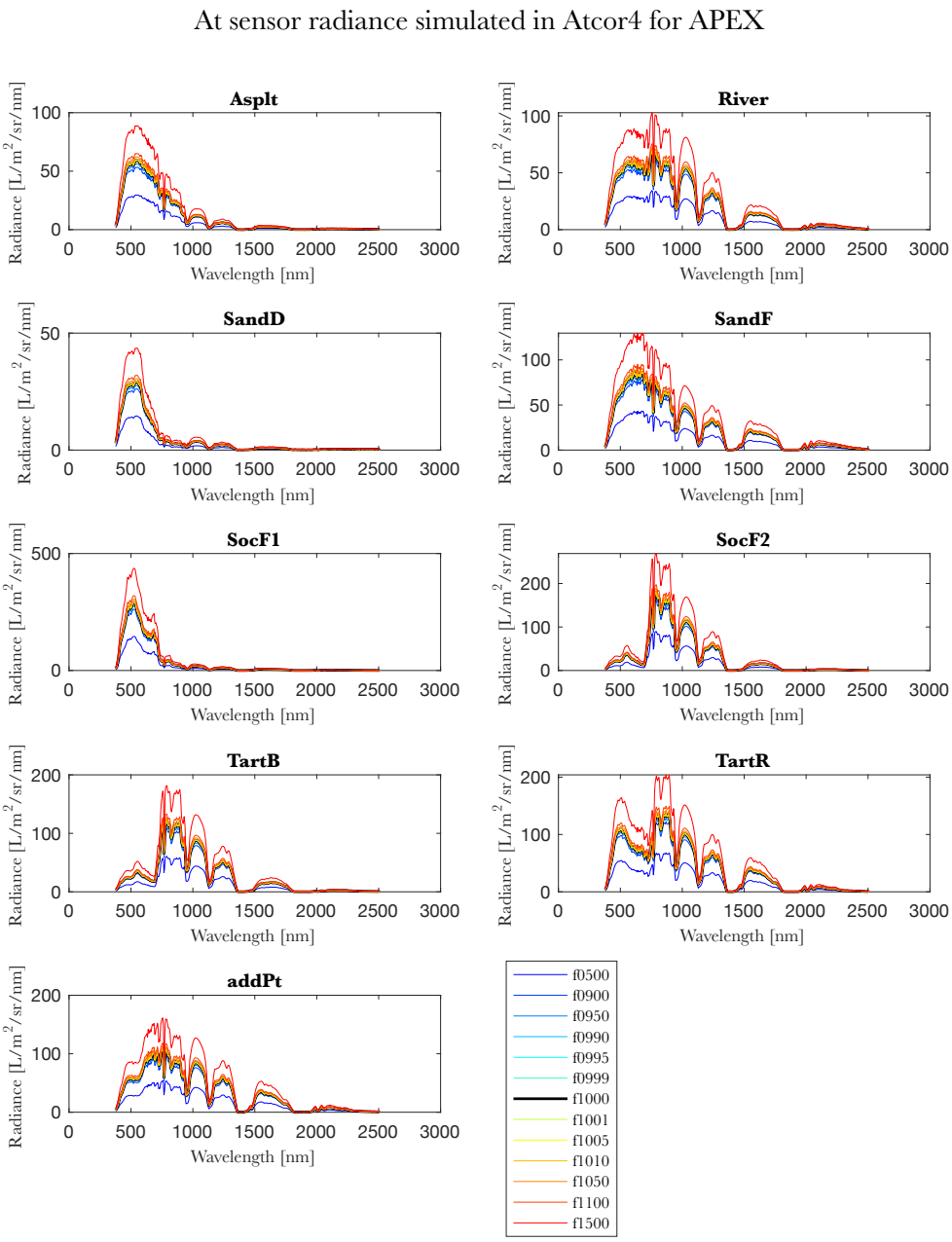

Figure 11: Simulated at-sensor radiances for a variety of ground refernce points. The factors are 50% ('f0500'), 90% ('f0900'), 95% ('f0950'), 99% ('f0990'), 99.5% ('f0995'), 99.9% ('f0999'), 100% ('f1000'), 100.1% ('f1001'), 100.5% ('f1005'), 101% ('f1010'), 105% ('f1050'), 110% ('f1100') and 150% ('f1500'). The data points are asphalt ('Asplt'), river ('River'), dark sand ('SandD'), fine sand ('SandF'), soccer field one in the centre of the image ('SocF1'), soccer field two at the edge of the image ('SocF2'), blue tartan ('TartB'), red tartan ('TartR') and an added pixel of a vegetation surface ('WatPt').

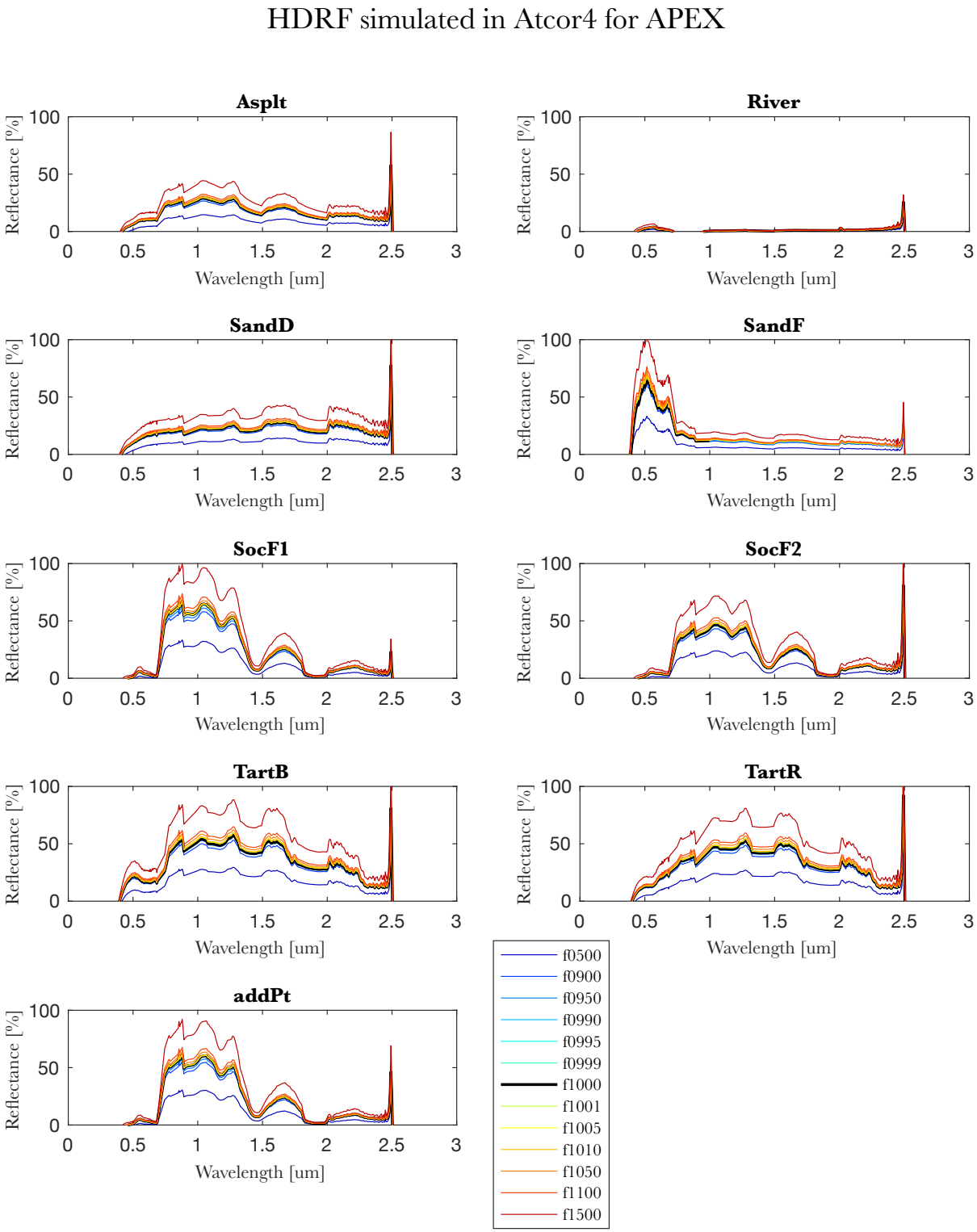

Figure 12: HDRF results in ATCOR-4 from simulated radiation intensities for APEX. Processed through Atcor4 as rugged terrain and without adjacency effect. The values in the legend refer to the factors for the input radiance. For example 'f0500' means 50%, 'f1000' represents the original or 'f1001' is equal to originally plus 0.1%. What can't be seen in this figure are the slightly negative values for values in the blue bands (lower than 400 nm).

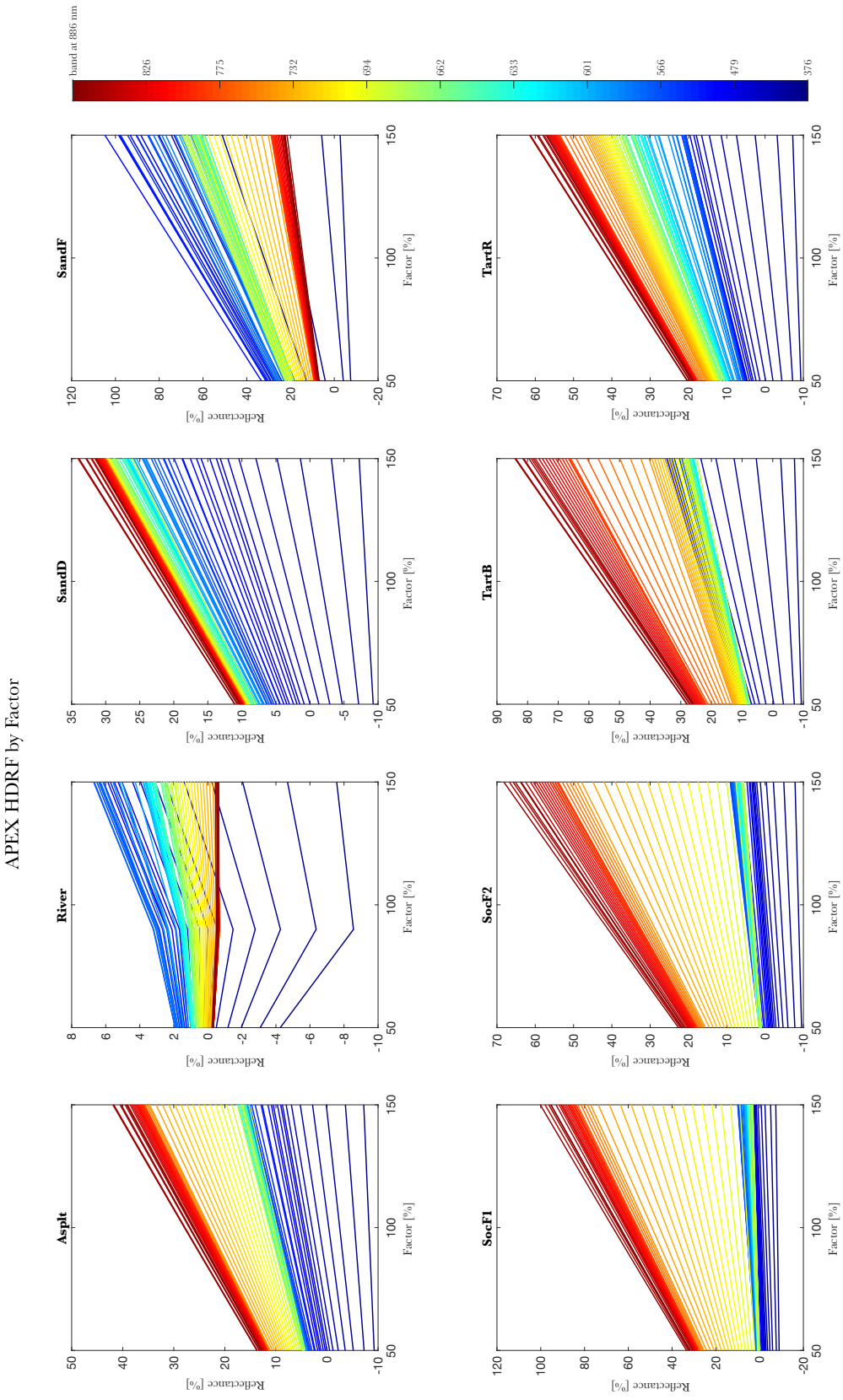

Figure 13: HDRF obtained for APEX by ATCOR-4 rugged terrain mode and 600 meters adjacency displayed as linear plots per radiance factor for each band between 367 and 886 nm (the first 100 bands).

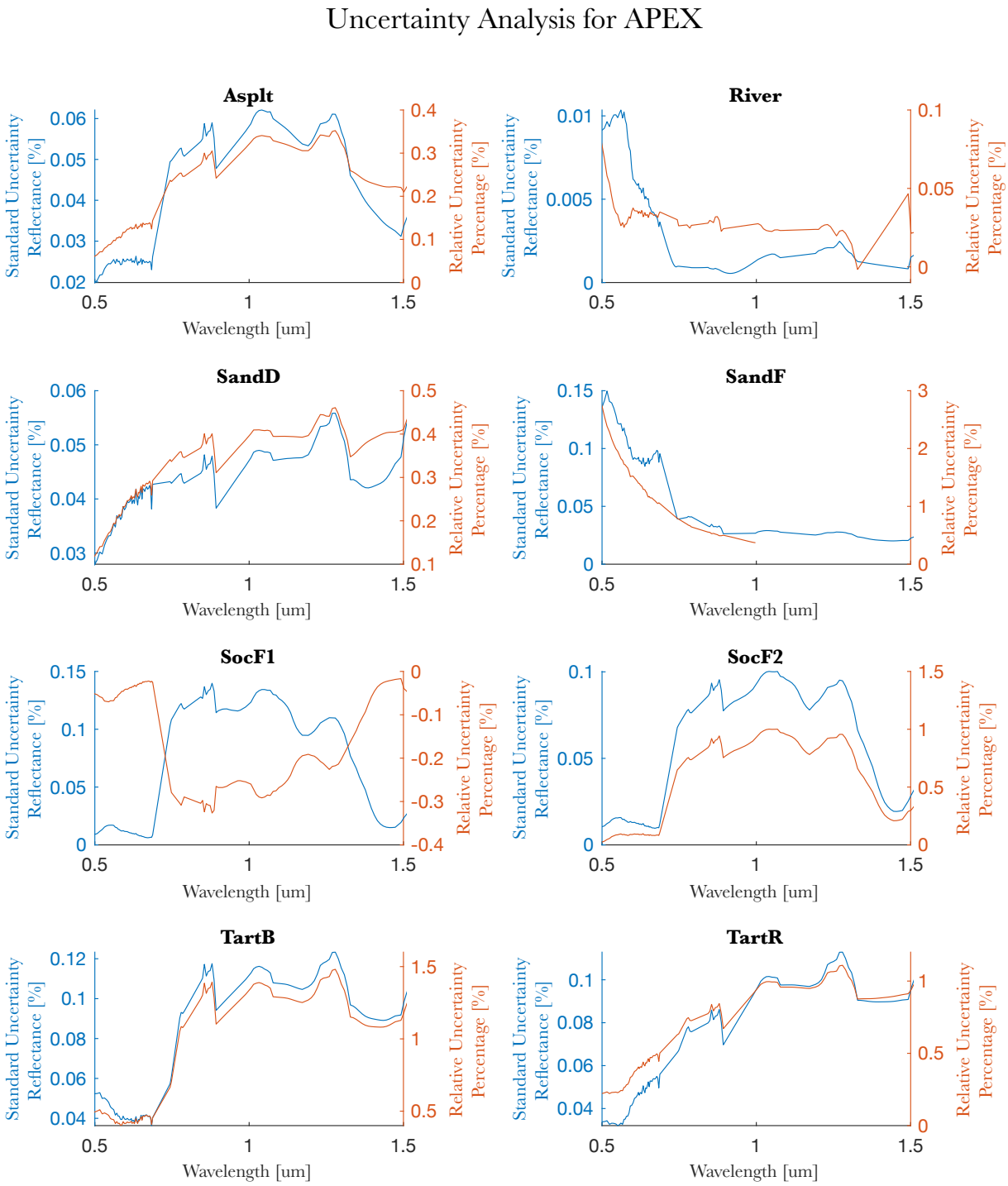

Figure 14: Absolute and relative uncertainty associated with the input radiance intensity for APEX in rugged terrain ATCOR-4 for wavelengths between 0.5 to 1.5 um. For some reason the dark sand surface shows a negative uncertainty while all the other surface types are in the positive range. The absolute uncertainty for blue bands aren't included in this illustrtion. They are much higher (up to 3%).

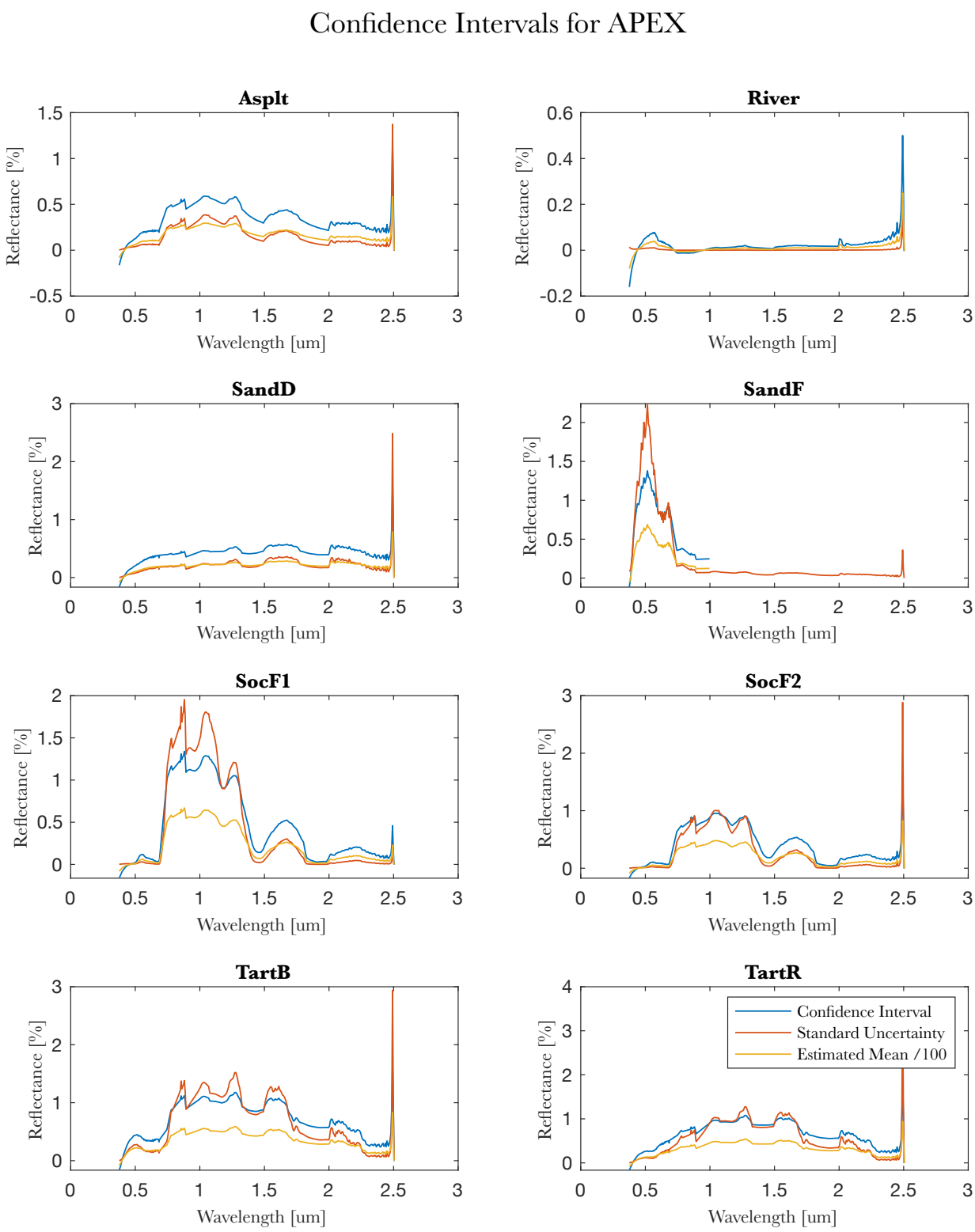

Figure 15: Comparison of confidence interval and standard uncertainty with additionally displayed estimated mean per wavelength divided by factor 100. The confidence level is 95%.

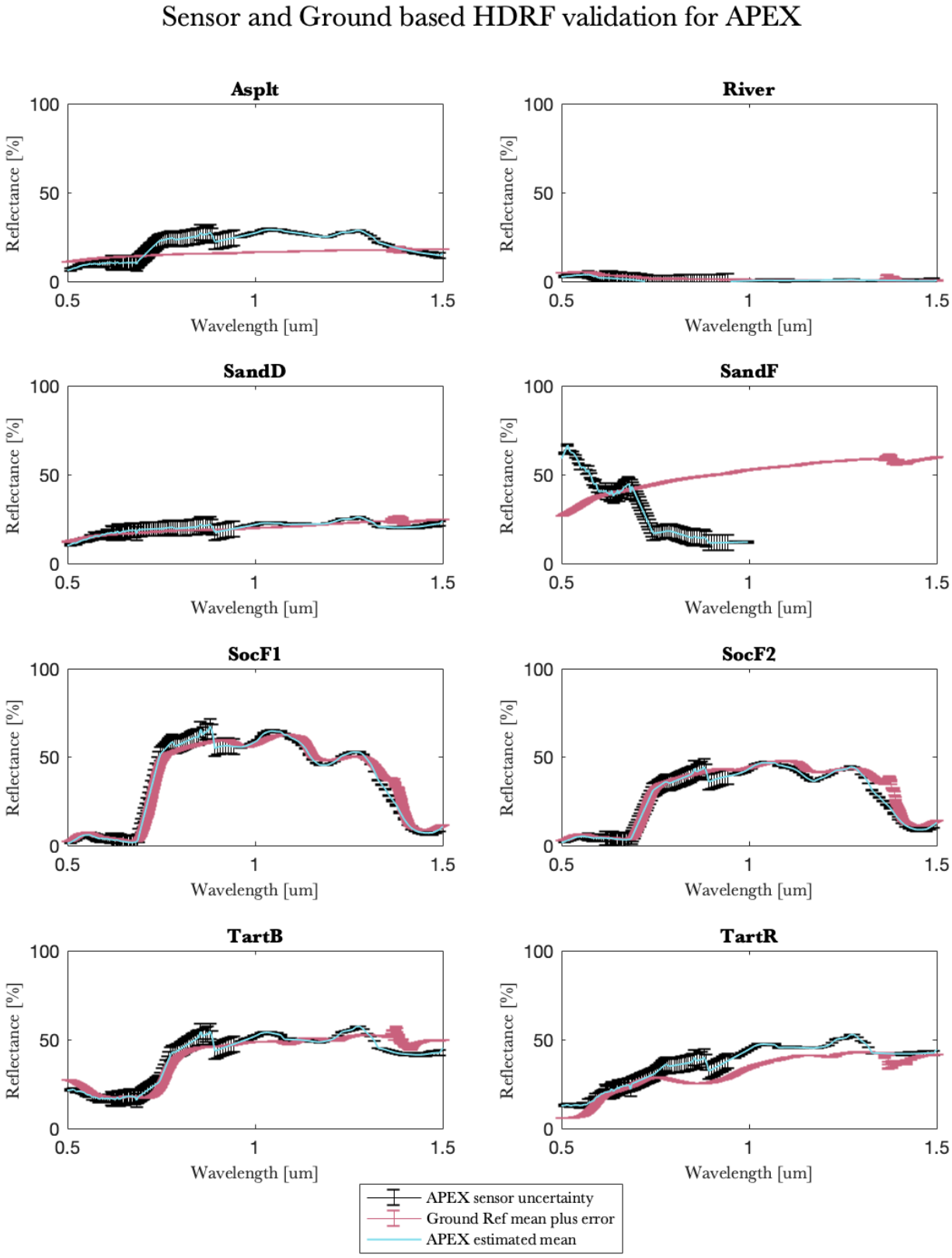

Figure 16: Uncertainty given by the instrumnet plotted with the estimated mean for the radiance input samples for ATCOR-4 and the ground field measurements including the given error.

The 95% confidence intervals presented in figure 15 contain one standard uncertainty over the entire spectrum for asphalt and dark sand. For river, soccer field two and red and blue tartan the standard uncertainty associated with variety in radiance intensity is mainly contained by the 95% confidence interval except for several bands. Soccer field one and fine sand have standard uncertainties higher than the 95% condfidence level for entire areas on the wavelength scale. It is clearly observable that the confidence level spectra as well follow the absorption features of the HDRF spectra.

To see how much of the variation could as well be caused by the instrument uncertainty of APEX (which is given by the spectral response function), figure 16 presents the estimated mean HDRF in addition and subtraction of the instrument uncertainty per wavelength. In comparison, the HDRF measured in the field is plottet against this range. For the river sample the ground mean plus error is within the mean airborne HDRF and its uncertainty range given by the sensor. For dark sand and the two soccer fields this statement is true as well for the visible to near infrared range. At higher band numbers the field HDRF of these surface types isn't necessarily within the airborne HDRF range. However, the sigma for the airborne estimations is lower at higher wavelngths because of the sensor composition. For the tartan surfaces the comparison shows similarities in shape of the spectra and location of absorption features but isn't accurate enough to be within the error range of the instrument. And then there are fine sand and asphalt who show very anomalous values.

4.2.2 Uncertainties associated with the choice of instrument type in ATCOR-4

In figure 17 the equivalent results for AVIRIS NG are presented for the reference points, an additional water point ('WatPt') and an additional agricultural surface ('AgrPt'). The reflectance spectra generally appear smoother compared to APEX. The connection between high radiance input and high differences in factorized HDRF is similar to APEX. The shapes of the spectra show surface specific features as the APEX results do. For blue tartan however, the spectra of factors 150% and 125% don't follow the pattern of the absorption feature at 1400 and 1900 nm. Other than that, no exceptions can be detected by eye.

Comparing the two sensors the main difference lays within the smoothness of the spectra. The HDRF spectra for AVIRIS NG are more homogeneous on a small wavelength scale. This is what one expects from a reflectance factor, since the reflectance properties are wavelength dependent but not necesserily highly sensitive on a nanometer level. Keeping in mind, that the APEX HDRF is taken before the iteration over the irradiane and the AVIRIS NG after the iteration, this might be a reason for the difference in smoothness. Another possible reason is the difference of flat versus rugged ATCOR-4. This case however will be discussed in a following section. The next paragraph describes the difference for the two sensors when both's HDRFs are calculated with flat terrain ATCOR-4.

In order to compare APEX and AVIRIS NG, figure 19 shows the mean HDRF per wavelength for each reference point for both sensors. For all surface types the last bands at 2500 nm show very high values for APEX whereas AVIRIS NG doesn't show these outliers. Again, the AVIRIS NG spectra are smoother at various wavelengths and surface types. Looking for example at the river surface, the AVIRIS NG spectrum is mainly at lower values than APEX and varies less between 2000 and 2500 nm. The same applies for fine sand but there the peak of APEX at 550 nm is shifted for AVIRIS NG to 450 nm. In the visible to near infrared the differences between the mean of the two sensors is several times 10% or higher. These differences are smaller for the soccer field surface types. Asphalt shows the same pattern of APEX being less homogeneous than AVIRIS NG.For the two tartan surfaces the APEX values are mainly 0-5% lower than AVIRIS NG. Here, the heterogenity on a small

scale of wavelength is not as different as for other surface points.

One of the reasons why the AVIRIS NG results are smoother HDRF spectra than APEX might be the interpolation that happens automatically for AVIRIS NG data in ATCOR-4. The APEX data on the other hand is not interpolated and likewise not post-processed in this example here. This means, with some spectral polishing, the APEX data might get closer to the AVIRIS NG spectra. However, for this analysis the important insight is, that data is being processed differently according to the instrument source.

Another interewsting comparison can be drawn between figure 13 for APEX and 18 for AVIRIS NG. The AVIRIS NG plot presents the lines per factor of radiance input for each instrument band between 377 and 1374 nm. Here, the general tendances again appear similar as higher HDRF values show higher slopes for the linear plots per factor. This is again given by simple mathematics. The observable shift in gradient around 620 nm is observable for fine sand, tartan and soccer field surfaces as well as the added agricultural pixel and the two water surfaces. Especially for the water surface points the break described for the water point in APEX is observable for AVIRIS NG as well. For the river pixel this break is more a saddle point and can be observed for every band. The water pixel has this break already at 90% and some ather anomalies between 95 to 99% for bands at wavlengths up to 700 nm. However, this break in linearity can be found for other surfaces too. For example blue tartan has it for its bands above 1300 nm or asphalt for bands below 450 nm. The low bands of the agricultural point and fine sand show the same pattern

In figure 20 the wavelengths 500 to 1500 nm are displayed for mean plus and minus sigma for APEX, AVIRIS NG and ADS respectively. Figure 20 is therefore a comparison of the obtained AVIRIS NG HDRF to the APEX HDRF while looking at the field reference measurments of the ASD field spectrometer at the same time. APEX with its 300 band has less bands within the same wavelength range than AVIRIS NG with over 400 channels. The AVIRIS NG sigma is generally about as large as the APEX uncertainty.

Looking at the different surface types, asphalt - which was detected as being significantly different to APEX - can be found to be very similar to the AVIRIS NG spectrum. The surface point with the least discrepancies among the three instruments is dark sand. When comparing the results of the two airborne sensors the APEX estimated mean generally lays within the range of the AVIRIS NG mean plus or minus sigma and the other way around the AVIRIS NG mean lays within the APEX mean plus or minus sigma for most cases. The same applies for the ground ASD measurements except for the fine sand pixel and generally the bands around 1800 to 1950 nm (not diplayed in figure 20). In this wavelength area the field measurements are anormally high and can though not be compared to the airborne values. This band area anyway is a water absorption feature and sometimes used as reference for the atmospheric compendation. So, the area of interest anyway is more towards the lower wavelengths. Especially, since - as presented in figure 11 this is where the many atmospheric effects mainly influence the measurements.

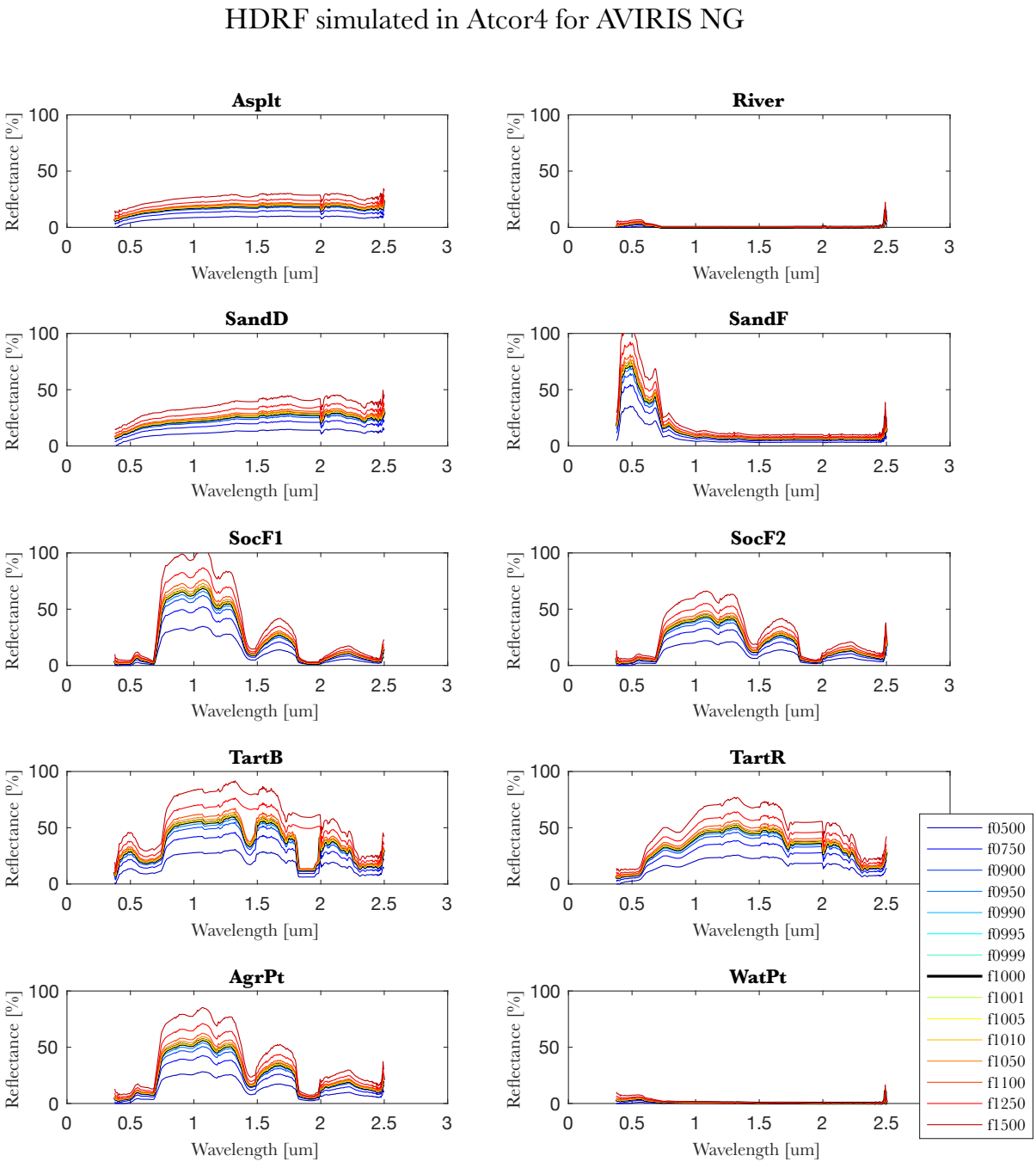

Figure 17: Simulated radiation intensities for AVIRIS NG. Processed through ATCOR-4 as flat terrain and with an adjacency effect of 600m accounted for. The factors are 50% ('f0500'), 75% ('f0750'), 90% ('f0900'), 95% ('f0950'), 99% ('f0990'), 99.5% ('f0995'), 99.9% ('f0999'), 100% ('f1000'), 100.1% ('f1001'), 100.5% ('f1005'), 101% ('f1010'), 105% ('f1050'), 110% ('f1100'), 125% ('f1250') and 150% ('f1500'). The data points are asphalt ('Asplt'), river ('River'), dark sand ('SandD'), fine sand ('SandF'), soccer field one in the centre of the image ('SocF1'), soccer field two at the edge of the image ('SocF2'), blue tartan ('TartB'), red tartan ('TartR'), an added agricultural pixel ('AgrPt') and an other added pixel of a water surface ('WatPt').

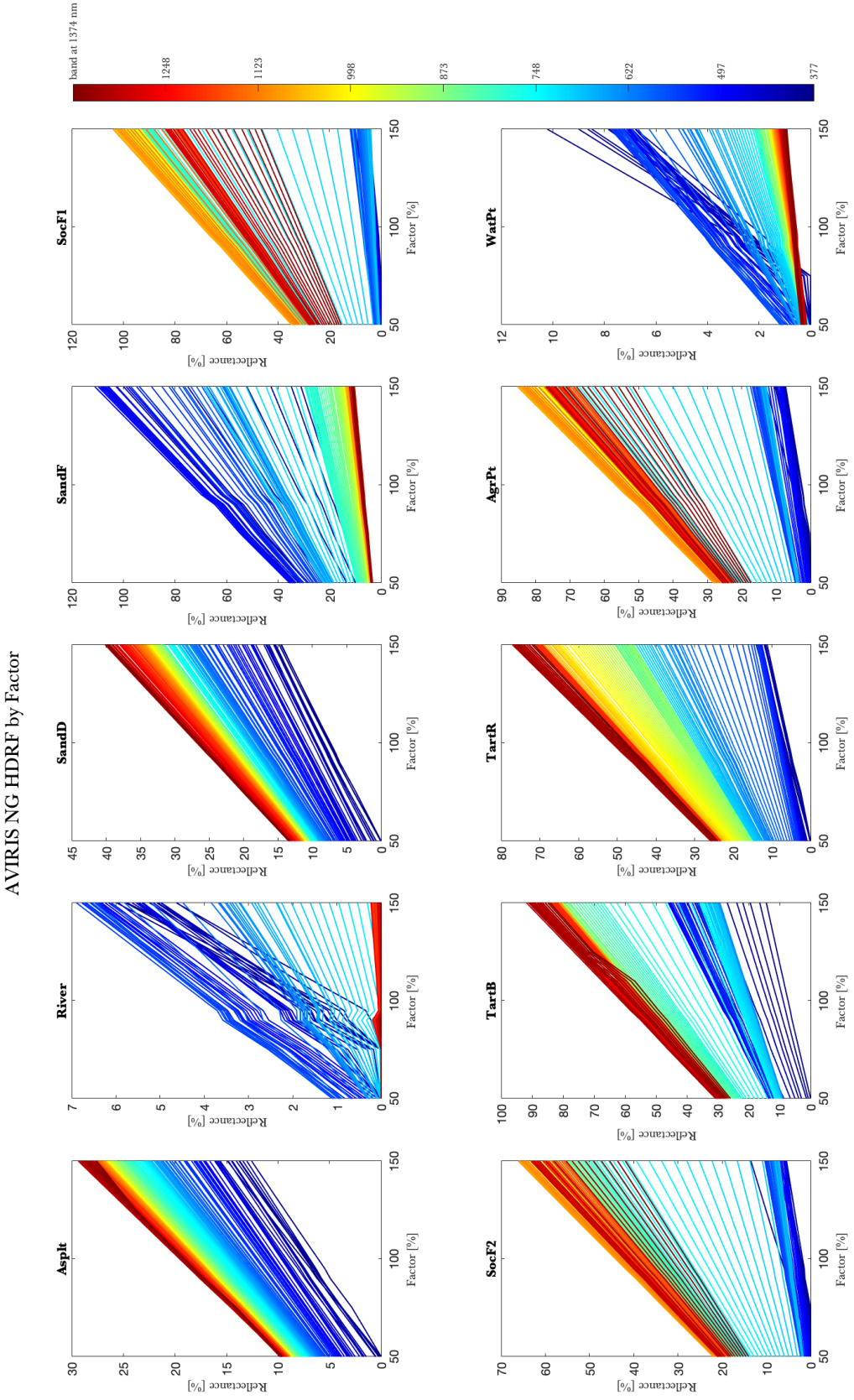

Figure 18: HDRF obtained for AVIRIS NG by ATCOR-4 flat terrain mode and 600 meters adjacency displayed as linear plots per radiance factor for each band between 367 and 886 nm (the first 200 bands).

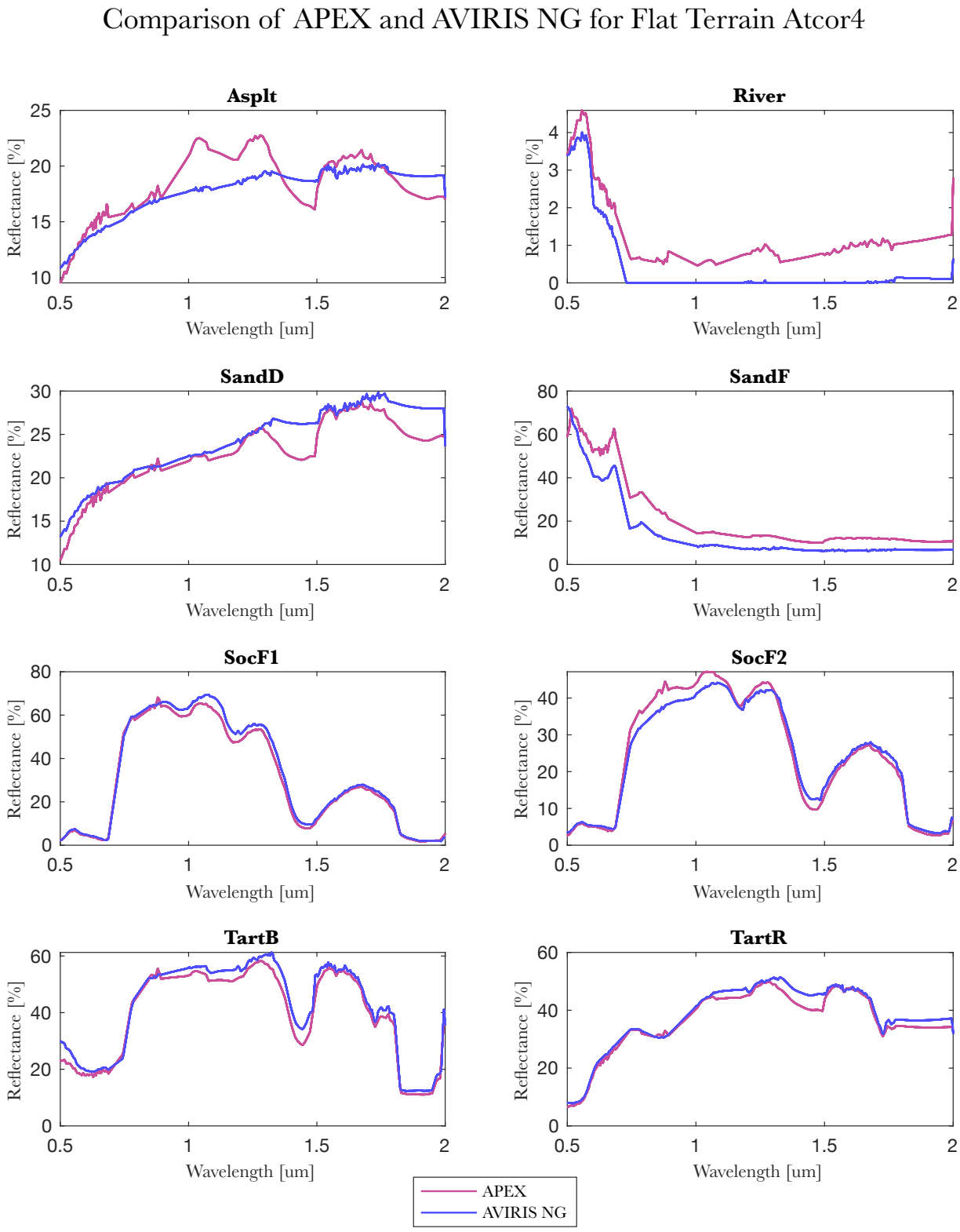

Figure 19: Comparison of the estimated mean for APEX and AVIRIS NG HDRF from ATCOR-4 processed as flat terrain for both sensors. Fine sand has very large differences. It might not be exactly the same pixel since for APEX this surface point is at the edge of the image. AVIRIS NG has higher HDRF results than APEX for the majority of surfaces and bands.

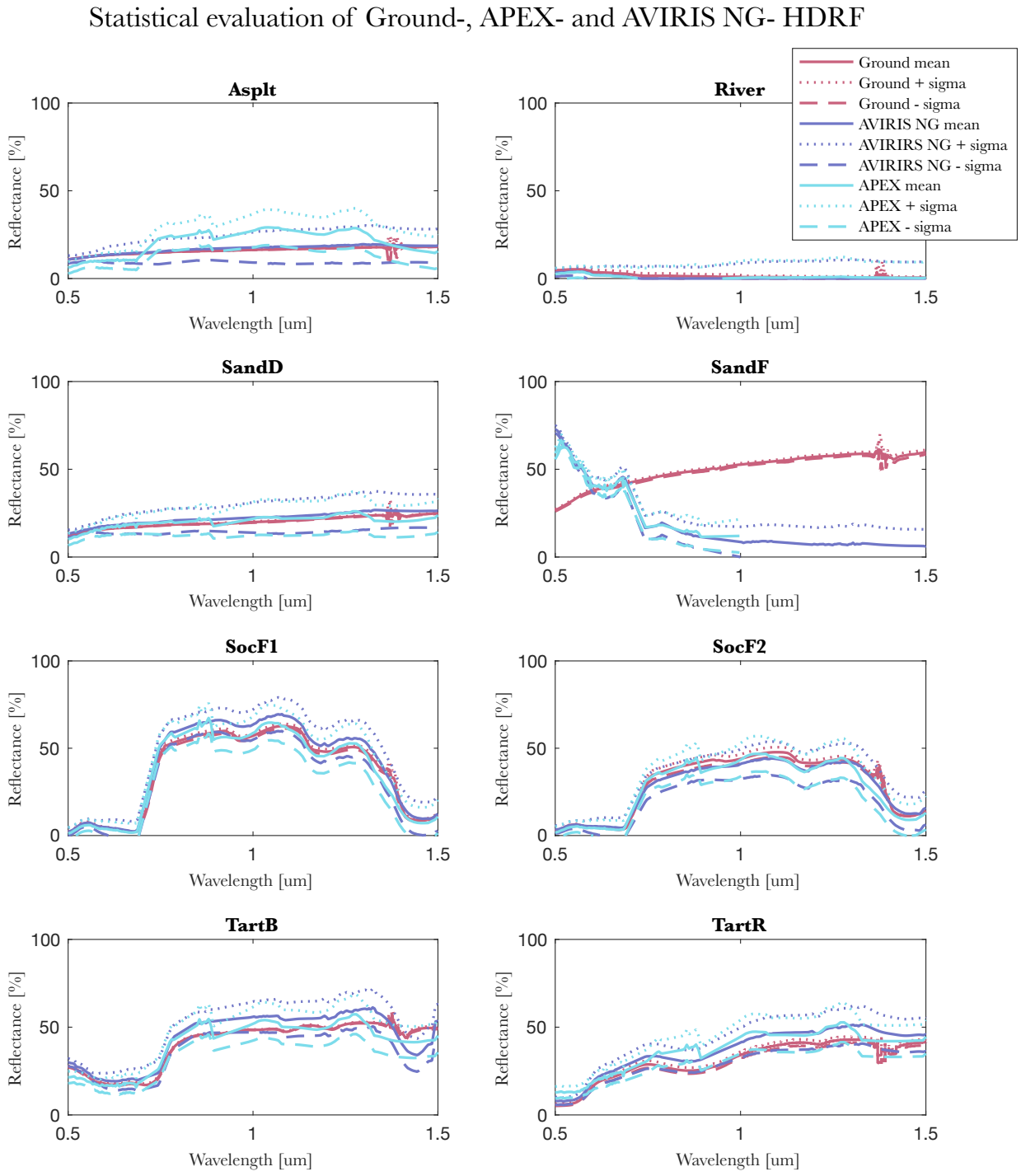

Figure 20: Estimated mean, estimated mean plus sigma and estimated mean minus sigma for APEX HDRF, AVIRIS NG HDRF and ASD field spectrometer HCRF. The wavelength area is 500 to 1500 nm. The upper uncertainty boundaries are marked by a dotted line, the lower sigma is represented by a dashed line and the estimated mean is a regular line. Fine sand shows a large discrepancy between the airborne and the ground data. This is most probably due to the fact, that the pixel is at the very edge of the airborne images and (pixel 1 across track).

4.2.3 Influence of the ATCOR-4 terrain mode

As mentioned, APEX HDRF eas obtained trough flat as well as rugged terrain mode in ATCOR-4. The difference between the results are presented in figure 21. All paramters were the same for those two spectra except for the fact, that the rugged terrain irradiance was estimated with an underlaying digital elevation model. The result differ most at the water vapor bands around 1400 and 1900 nm. There, the rugged terrain mode interpolates over the absorption features. The band depth is genrally lower and the spectra from rugged terrain atmospheric compensation look smoother. For soccer field two the flat terrain HDRF is genrally lower than the rugged terrain HDRF. Asphalt has a wavelength range around 1000 nm where the rugged terrain HDRF is underestimated compared to flat terrain. Blue tartan shows an overestimation for rugged compaired to flat terrain at 700 nm. And for all surface types the flat terrain mode isn't able to compensate for the outliers at 2500 nm.

4.2.4 Uncertainty associated with adjacency effects

As mentioned, a significant portion of the total radiance arriving at the sensor comes from adjacent areas. Within the same terrain mode and after running the complete atmopsheric compensation the question still remains how much the adjacency range influences the output. This question is answered in figure 22. The ranges of zero and 600 meters adjacency effect were chosen as samples. When looking at figure 22 it becomes clear that not accounting for the adjacency effect can have large impacts on the resulting spectra in the atmospheric compensation. Especially for HDRF values above 50% the estimation with adjacency effect is up to 5% reflectance larger than with no adjaceny effect (zero meters adjacency).

Again, the strength of the effect is wavelength and surface type dependent. Looking at absolute values, for fine sand, soccer field one and blue tartan the difference is the largest. For the soccer fields and sand the difference in % between the spectrum with adjacency to the one without is highest around 800 to 1300 nm. For blue tartan the 600 meters adjacency HDRF takes higher values than the zero meters HDRF over the entire spectrum. River and asphalt show negative differences at several band areas. The relative differences tend to be highest at the visibible to near infrared range for all surface types. For the river pixel the realtive difference is up to minus 0.2%. The soccer fields show values in the same range around 500 nm. Dark sand has a posistive relative difference in the visible range with values up to 0.1%.

Figure 23 presents the absolute difference in reflectance for the HDRF before and after the irradiance iteration. Since this is when the adjacency effect ijs included in the process, figure 23 presents very well how the spectra would look without accounting for scattering from neighbouring areas at all. Clearly, there is a differnece between no adjaceny in 22 and before the final processing steps in 23. Interstingly, the difference between the first reflectance estimation and the finally estimated HDRF is quite similar to the difference of flat to rugged terrain mode. The uncertainty associated with the adjacency effect can be divided into two aspects. To not account for uncertainty at all while not iterating over the estimated irradiance values and taking the first guessed reflectance factor as the result is as inaccurate as switching the terrain mode. Not accounting for adjacency by using a zero meters range of influence is as well producing systematic errors. The range of the error is in a 0.1% range. This might appear very small but can still have a larger influence, especially for refelctance values of higher magnitude.

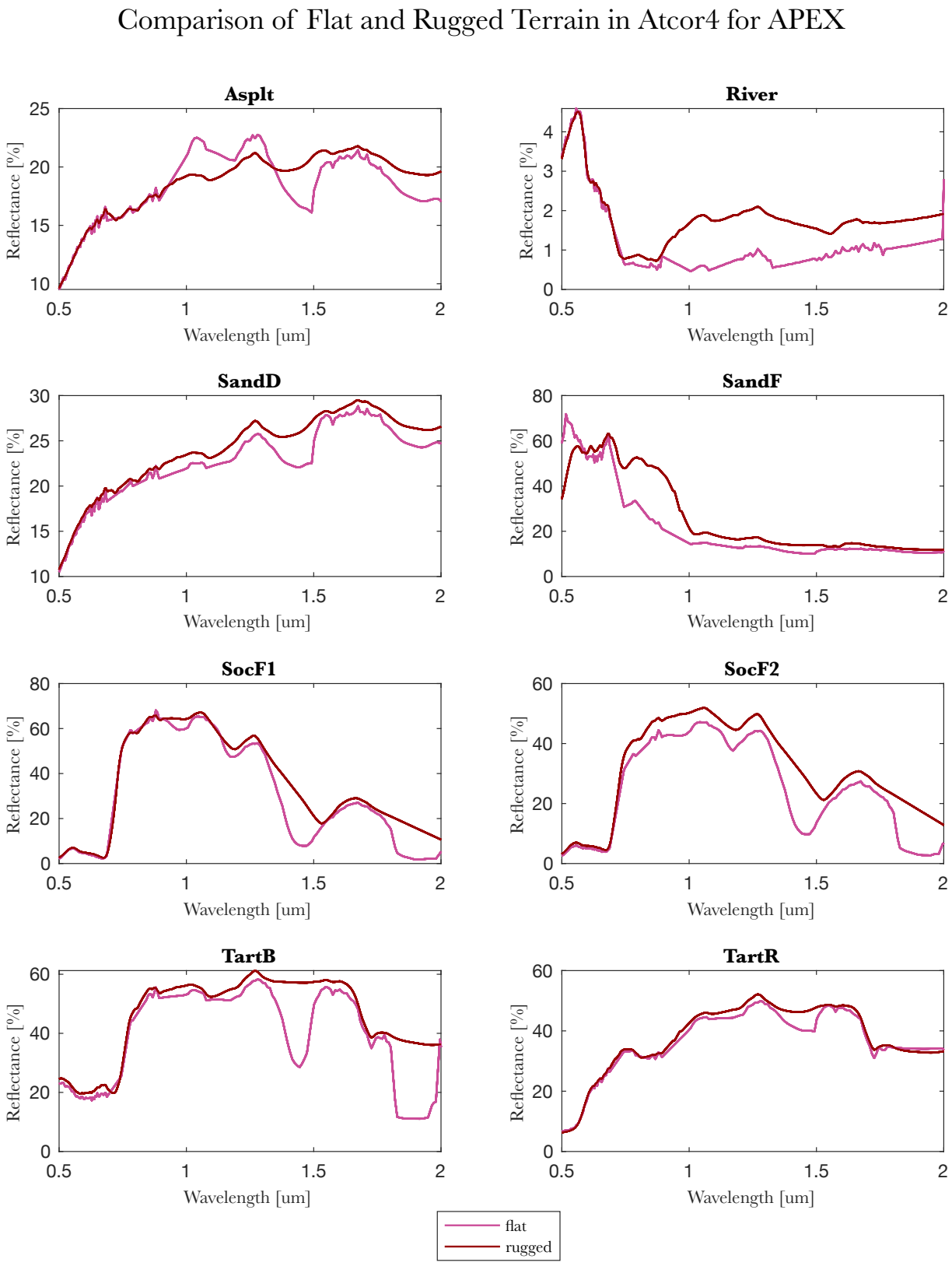

Figure 21: Comparison of APEX HDRF produced by ATCOR-4 in flat and rugged terrain mode.

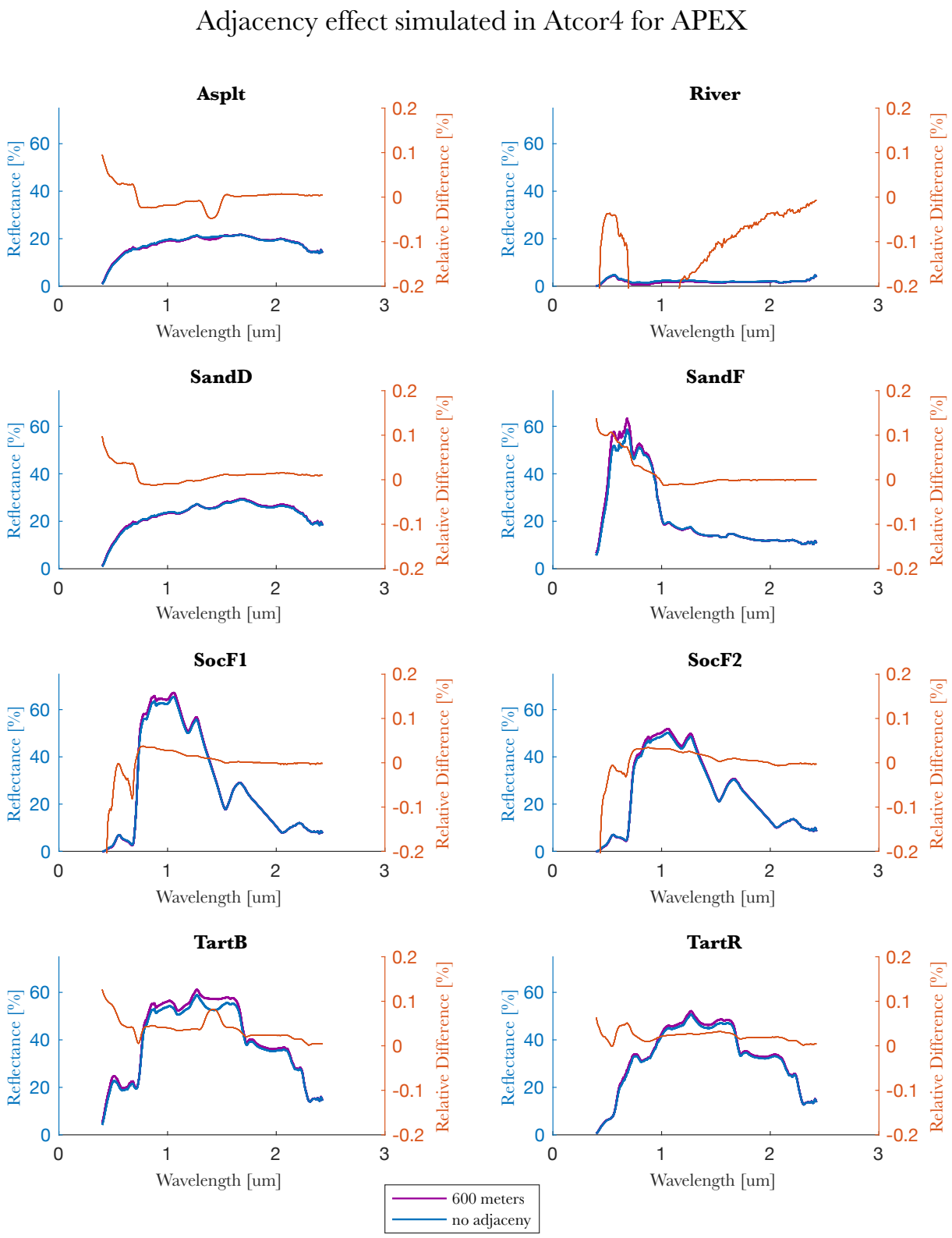

Figure 22: Illustration of the impact the adjacency radiance has on the APEX HDRF produced by ATCOR-4 rugged terrain. One image is calculated with no adjacency effect (zero meters), the other image is calculated with an adjaceny range of 600 meters.

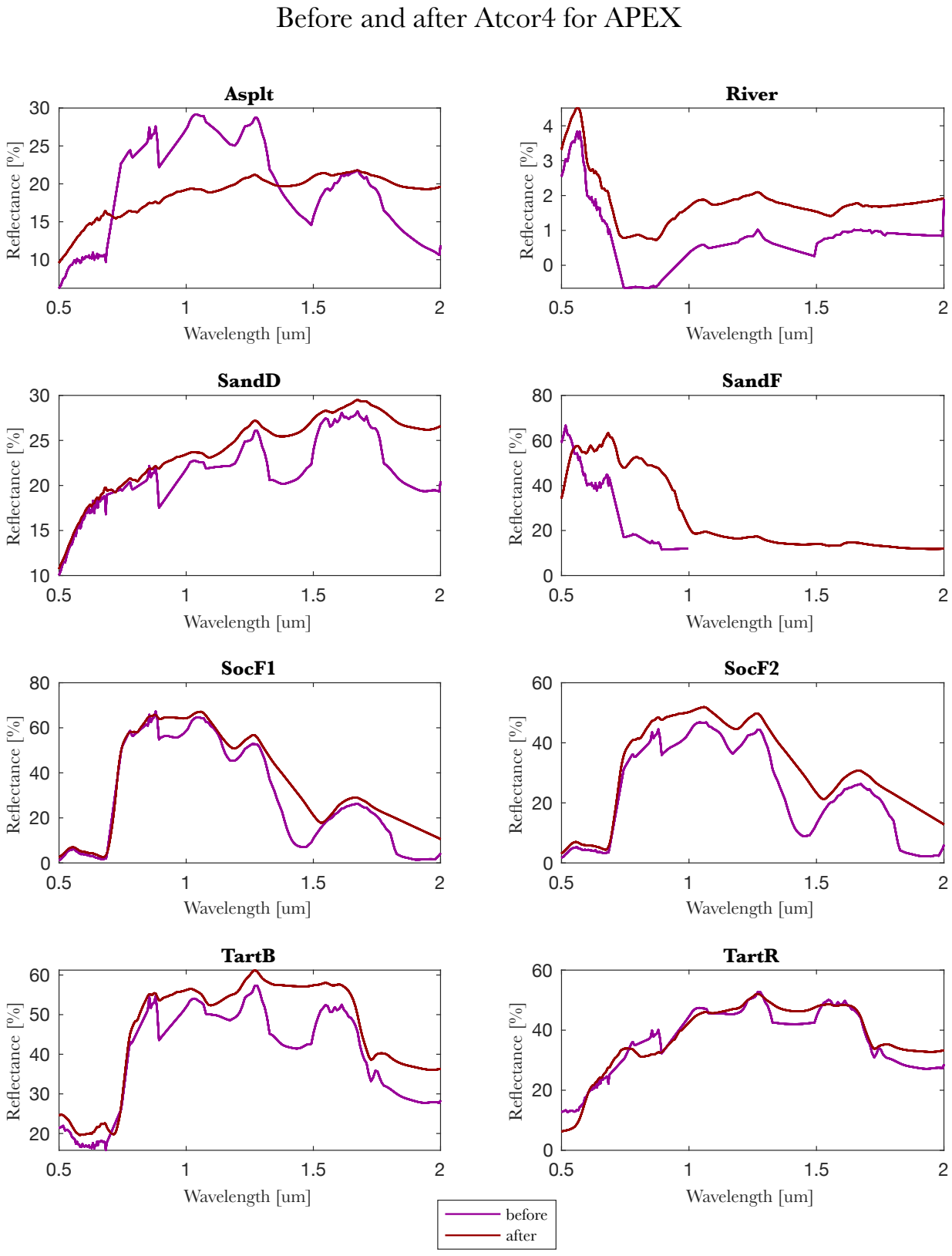

Figure 23: Difference between first reflectance estimation and final ATCOR-4 rugged terrain product with 600 meters adjacency included.

5 Discussion

The collection of aspects influencing the result of the atmospheric compensation presented above is far from complete. The absolute ranges of uncertainty presented in the section above go up to 20% for certain effects. The relative uncertainties don't exceed 1.5% for the variables presented above (except for the fine sand surface). When comparing these values to the study of Hueni et al. (2016) it is possible to range those values. As a relative standard deviation for the radiance values who serve as input to the atmospheric compensation a value of 6.8% is suggested for APEX. Comparing that value to the applied factors in this study here, it would be in the range of 90 to 95% and 105 to 110% respectively. The reflectance values for these factors are just around the break in linearity for water pixels. Generally, the maximum 1.5% uncertainty for certain surface types don't seem very high. On the other hand, when comparing it to Thompson's et al. (2018b) total 1% it is quite a lot for ATCOR-4 since systematic effects still need to be added. However, the AVIRIS NG uncertainty values in this study done with ATCOR-4 anyway can't be compared to the results of the Thompson study since the data and surface types are completely different.

In general, the uncertaints associated with the input radiance intensity for the atmospheric compensation in ATCOR-4 is depending on the surface type and wavelength. For vegetation pixels the atmospheric compensation is by trend more accurate and therefore the radiance values are transformed less arbitrarily. On the other hand water pixels have their main reflectance properties in lower bands where ATCOR-4 is struggling anyway and additionally are the generally lower values more sensitive to errors (the same absolute error for a low value is relatively more significant than for a higher value). The absolute uncertainty for the those bands below 0.4 um is 3 to 4%. So, for a radiance value like 0.1 the reflectance can quickly turn into a negative value.

It is possible that the affected bands or surface points were overcalibrated in the course of the aerosol estimation or even accidently taken as shadow pixels. It seems likely that the contrast of the image might have an influence on the way it is processed. There is an option in ATCOR-4 at the point where the thresholding for dark pixels take place, when the mode of contrast stretching can be chosen (either Gaussian or by histogram). In this study every threshold was produced by gaussian fitting. For the radiance images with higher factors the standard deviation in brightness was higher, so the thresholding of shadow pixels must have been less uncertain. There might exist an uncertainty associated with the general contrast of the image. Therefore, the question would be how much of the entire uncertainty for the radiance that serves as input to the compensation are caused by systematic errors for the sensor. This question can partly be answered by the fact that the FWHM is increased for bands at wavelengths higher than ca 950 nm. So, for higher band numbers the systematic effect might be larger. Then again many dark pixels are water and this surface type basically has zero reflectance at higher band numbers.

The comparison of APEX, AVIRIS NG and ASD HDRF showed that the uncertainty of the bands in wavelength areas higher than 1 um are still mainly overlapping for the three sensors. But as seen in the differrent parts of the result section, the processing step, the adjacency range and the terrain mode can change the way the spectra appear very much. So, the choice of the sensor will influence the type and scale of the systematic effects in the uncertainty analysis. Also, the assumption of independence for the uncertainty per wavelength might per se not be accurate since the bands are chosen in clusters and spectral interpolation is applied for where the sampling pattern has gaps. For the uncertainty values concerning wavelength dependent sigmas the systematic effect might need to be modelled with errors from the spectral fitting process. It is to assume, that within the atmospheric compensation algorithm wavelength dependent systematic errors occure too. Not

only the high uncertainty for the first bands in the blue area need to be analysed seperately. An example herefore would be the bands that were used for the water vapor retrieval (in this study it was the 940 nm region).

As observed, two parts of the uncertainty associated with the radiance are caused by the choice of reference spectrum and the exact date and time chosen for the calculation of solar zenith and azimuth angle. The evaluation of the reference spectrum aspect didn't result in standard uncertaitny values due to the fact that it was a comparison between two models. Still, if one was to find a number of uncertainty (per wavelength) it would have to be added in quadrature to the already existing standard uncertainty. The uncertainty associated with the zenith and azimuth angle problem on the other hand is part of the combined standard uncertainty because the irradiance model doesn't change. Therefore, the uncertaitny associated with the solar angles might be included as a systematic effect only by looking at the covariance of irradiance and geometry. Again, we don't have a definitive number since the estimation of this uncertainty value would need more data in the form of different campaigns.

Of course, the choice of water vapor region, the sensor model (spectral calibration file), spatial resampling or geometric uncertainties could all influence the HDRF as well and might even have covariances associated with the input radiance intensity. Even the look up table MODTRAN could actually be compared to another one as for example LIBRATRAN. It is however save to assume that at least some of those effects (no claim for completeness) cancel themselves out. Their associated uncertainty could actually be modelled. However, the uncertainties that are far more difficult to model are the covariances. It might though not be necessary to find all joint probability distributions since at the end the aim is to provide a product with preferrably one uncertrainty value associated with it. It is then secondary how this value is composed. The primary concern should be to be consistent in the use of models and modes and unambiguous in terminology.

6 Conclusion

As a result the case study showed how the radiance intensity has an associated uncertainty of 0 to 1.5% per wavelength when processed through ATCOR-4 for APEX and AVIRIS NG. The two sensors's sigmas mainly include the reference measurements in the field by an ASD spectrometer. For how many and which bands the standard deviation of APEX lays within the 95% confidence interval strongly depends on the surface type. The uncertainty analysis can be extended to systematic errors that are mainly wavelength dependent. Also, during the implementation of the atmospheric compensation correlating uncertaitny might be introduced trough making assumptions and choices concerning processing mode and parameters. For example between the radiance values and the solar zenith and azimuth angle exists a relation. Other examples are the solar irradiance reference spectrum chosen, the terrain mode in ATCOR-4, the adjacency range in ATCOR-4 or generally the choice and calibration of the sensor.

To understand the ongoing uncertainty processes is important in order to make different studies comparable to each other and to once extend atmospheric compensation algorithms on other regions where ground reference measurements might be less accessable. The importance of finding accurate definitions, correlations and systematic uncertainties states how comlex radiative transfer modelling is. This thesis is an attempt to capture a wide and multilayered picture. The aspects discussed were:

- The unclear definition of the unit area $dA_{\perp}$ is an example for a gap in terminology.
- The solar irradiance reference model can be a source of systematic errors.
- Approximations of the solar zentih and azimuth angle for the entire image even though the values change by time and space have significant systematic uncertainty potential.
- Systematic effects occur in the form of sensor uncertainty due to instrument charcteristics.
- The intensity of the radiance as indicator of general image contrast and therefore sensor calibration is a source of uncertainty associated with the atmospheric compensation process.
- Wavelength dependent effects due to the performence of ATCOR-4 in the blue range can be seen as a source of corrrelation when searching for combined uncertainties.
- Sensor dependent HDRF values for ATCOR-4 indicate systematic biases within the algorithm.
- The choice of terrain mode in ATCOR-4 influences the resulting HDRF as much as stopping the process after the first irradiance iteration.
- The uncertainty associated with the adjacency range is non-negligible and wavelength and surface dependent as well.

The list above is not complete. The selection of variables as well as the extent of their description and quantificaiton of their uncertainty can be widely expanded. In a future step one could calculate absolute and relative uncertainties for basically every factor involved in the atmospheric compensation process and complete this uncertainty analysis to the detail. This, however, might be a waste of time and resources. First of all, the technology is evolving and it makes more sense to investigate in generally less uncertain methods that can be applied on more surface regions than to analyse this one method over and over even though it might not

be used anymore in twenty years. Anyway, it is certainly important to have those critical uncertainty factors in mind when thinking about new approaches. Maybe they can even be used as a first step towards a new idea.

Secondly, there is always an uncertainty associated - even with the uncertainty. So, another aspect to think about would be how to make uncertainty analysis more uniform and also more mandatory. The GUM is certainly helpful to find values in order to number the uncertainty associated with results and to encourage appropriate traicability management. But the question arises, how to actually use those values in a comparison of different methods, study sites or surfaces. The uncertainty might be numbered, but it always has to be seen relative to its setting. As mentioned, we don't know the truth. We can only do estimations. So, one might say that the uncertainty associated with the HDRF for a surface type 'a' or method 'A' is estimated lower than for surface 'b' or method 'B'. But in the end both methods might have the same underlying false assumption or the same gap in the methodology of the measurement. An uncertainty analysis is quantifying how much the phenomenon that is measured accords with the models and concepts we have about it. Therefore, it would be foolish to assume that an uncertainty analysis does not as well has an unknown error.

References

Berk, A., et al., 2014. Modtran®6: a major upgrade of the Modtran® radiative transfer code. pp. 1-4.

Bernstein, L. S., et al., 2005. Validation of the QUick Atmospheric Correction (QUAC) algorithm for VNIR- SWIR multi-and hyperspectral imagery. Defense and security, International Society for Optics and Photonics, pp. 668-678.

Committee for Guides in Metrology, 2008. Evaluation of measurement data - Guide to the expression of uncertainty in measurement. Report JCGM 100:2008.

Fontenla, J. M., et al., 2011. Highâresolution solar spectral irradiance from extreme ultraviolet to far infrared. Journal of Geophysical Research, vol. 116 (D20108), pp. 1-31.

Gao, B.-C., et al., 2009. Atmospheric correction algorithms for hyperspectral remote sensing data of land and ocean. Remote Sensing of Environment, vol. 113, pp. S17-S24.

Hueni, A., et al., 2012. D1.4-1.7 Spectral Calibration (of APEX) by RSL (University of Zurich, Department of Geography).

Hueni, A., et al., 2016. Field and Airborne Spectroscopy Cross Validation - Some Considerations. Journal of selected topics in applied earth observation and remote sensing, vol. 10(3), pp. 1117-1135.

Kruse, F.A., 1988. Use of airborne imaging spectrometer data to map minerals associated with hydrothermally altered rocks in the northern Grapevine Mountains, Nevada and California. Remote Sensing of Environment, vol. 24, pp. 31-51.

Kuekenbrink, D., et al. 2018. Mapping the irradiance field of a single tree: quantifying vegetation induced adjacency effects Transactions in Geoscience and Remote Sensing (Draft).

Reinersman, P. N., et al., 1998. Satellite-sensor calibration verification with the cloud-shadow method. Applied Optics, vol. 37(24), pp. 5541-5549.

Richter, R., 1998. Correction of satellite imagery over mountainous terrain. Applied Optics, vol. 37, pp. 4004-4014.

Richter R. and Schläpfer D., 2002. Geo-atmospheric processing of airborne imaging spectrometry data. Part 2: Atmospheric/Topographic Correction. International Journal of Remote Sensing, vol. 23(13) pp. 2631-2649.

Richter R. and Schläpfer D., 2016. ATCOR-4 User Guide, Version 7.0.3.

Roberts, D.A., et al., 1986. Comparison of various techniques for calibration of AIS data. Vane G, Goetz AFH (eds) Proceedings of the 2nd Airborne imaging spectrometer data analysis workshop, JPL Publication, Jet Propulsion Lab, Pasadena, vol. 86-35, pp. 21-30.

Rodgers, C. D., 2000. Inverse methods for atmospheric sounding: theory and practice volume 2. World scientific.

Schaepman-Strub, G., et al., 2006. Reflectance quantities in optical remote sensing - definitions and case studies. Remote Sensing of Environment, vol. 103, pp. 27-42.

Schläpfer D., 2011. MODO User Manual, Version 5. ReSe.

Schläpfer D., Hueni, A. and Richter, R., 2018. Cast Shadow Detection to Quantify the Aerosol Optical Thickness for Atmospheric Correction of High Spatial Resolution Optical Imagery. Remote Sensing, vol. 10(200), pp. 1-25.

Thompson, D. R., et al., 2018a. Retrieval of Atmospheric Parameters and Surface Reflectance from Visible and Shortwave Infrared Imaging Spectroscopy Data. Surveys in Geophysics, Springer Nature B.V., pp. 1-28.

Thompson, D. R., et al., 2018b. Optimal estimation for imaging spectrometer atmospheric correction. Remote Sensing of Environment, Remote Sensing of Environment, vol. 216, pp. 355-373.

Thompson, D. R., et al., 2019. A unified approach to estimate land and water reflectances with uncertainties for coastal imaging spectroscopy. Remote Sensing of Environment, vol. 231, pp. 1-18.

Thuillier G., et al., 2002. Solar irradiance reference spectra for two solar active levels. Advances in Space Research, vol. 34(2004), pp. 256-261.

Appendix

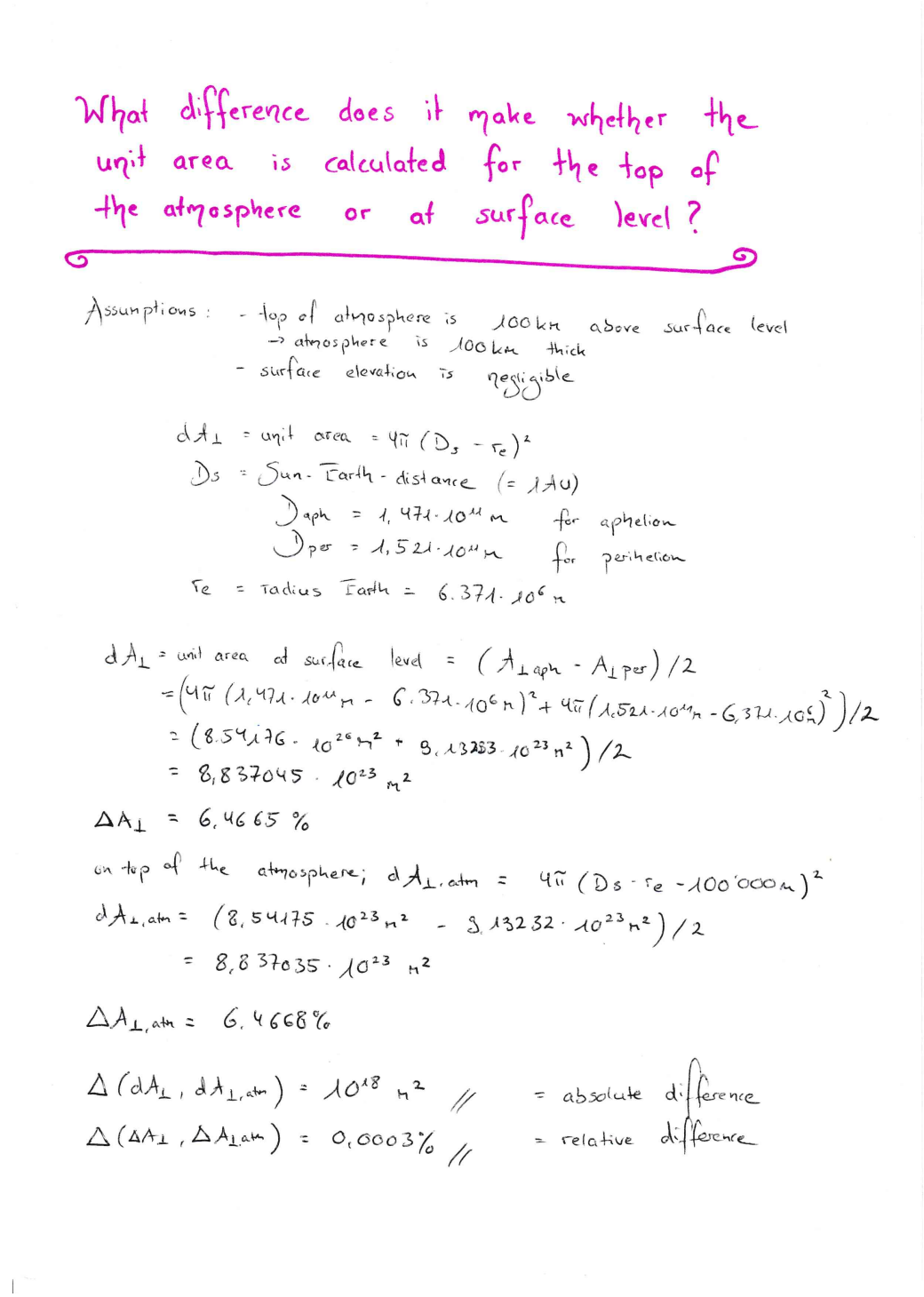

Figure 24: Calculations of the differences between unit area with and without consideration of the atmosphere.

Science Pledge

Personal declaration: I hereby declare that the submitted thesis is the result of my own, independent work. All external sources are explicitly acknowledged in the thesis.

Binz, 30.9.19